AD-A120 388 ATMOSPHERIC SCIENCE ASSOCIATES BEDFORD MA F/G 7/4
TECHNICAL STUDIES IN SUPPORT OF THE DESIGN OF A CLOUD WATER CON--ETC(U)
JUL 82 H G NORMENT F1962A-81-C-0124
UNCLASSIFIED AFGL-TR-82-018A NL

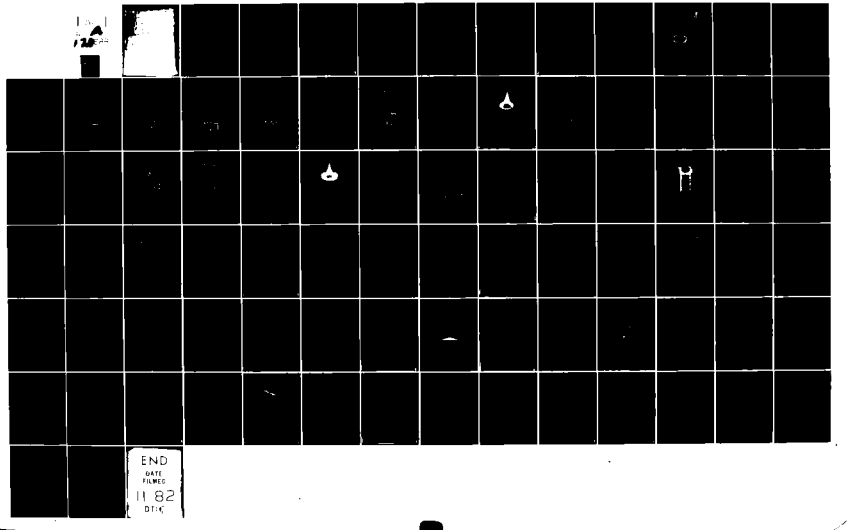

Unclassified

SECURITY CLASSIFICATION OF THIS PAGE *(When Data Entered)*

REPORT DOCUMENTATION PAGE		READ INSTRUCTIONS BEFORE COMPLETING FORM
1. REPORT NUMBER AFGL-TR-82-0188	2. GOVT ACCESSION NO. AD-A120 388	3. RECIPIENT'S CATALOG NUMBER
4. TITLE *(and Subtitle)* TECHNICAL STUDIES IN SUPPORT OF THE DESIGN OF A CLOUD WATER CONTENT METER AND HYDROMETEOR SPECTROMETER		5. TYPE OF REPORT & PERIOD COVERED Scientific - Final 6/12/81 - 6/11/82 6. PERFORMING ORG. REPORT NUMBER
7. AUTHOR(s) Hillyer G. Norment		8. CONTRACT OR GRANT NUMBER(s) F19628-81-C-0124
9. PERFORMING ORGANIZATION NAME AND ADDRESS Atmospheric Science Associates 363 Great Road; P.O. Box 307 Bedford, Massachusetts 01730		10. PROGRAM ELEMENT, PROJECT, TASK AREA & WORK UNIT NUMBERS 62101F 667012BC
11. CONTROLLING OFFICE NAME AND ADDRESS Air Force Geophysics Laboratory Hanscom AFB, Massachusetts 01731 Contract Monitor: Mr. Anthony Matthews (LYC)		12. REPORT DATE 10 July 1982 13. NUMBER OF PAGES 83
14. MONITORING AGENCY NAME & ADDRESS *(if different from Controlling Office)*		15. SECURITY CLASS. *(of this report)* Unclassified 15a. DECLASSIFICATION/DOWNGRADING SCHEDULE

16. DISTRIBUTION STATEMENT *(of this Report)*

Approved for public release; distribution unlimited

17. DISTRIBUTION STATEMENT *(of the abstract entered in Block 20, if different from Report)*

18. SUPPLEMENTARY NOTES

19. KEY WORDS *(Continue on reverse side if necessary and identify by block number)*

cloud water content
cloud water content meter
hydrometeor spectrometer

20. ABSTRACT *(Continue on reverse side if necessary and identify by block number)*

Theoretical, computational and literature survey studies in support of the design of novel airborne cloud water content and hydrometeor spectrometer instruments are reported. Measurements depend on momentum effects of impacted hydrometeors that are retained temporarily on flat, annular, rotating surfaces mounted normal to the airplane flight path.

DD FORM 1 JAN 73 1473

Unclassified

SECURITY CLASSIFICATION OF THIS PAGE *(When Data Entered)*

20.

The studies are of three types: 1. calculation of flow fields and water drop trajectories; 2. analyses of dynamic pressure distributions across, and total torque on, the vanes which rotate the annuli; and 3. hydrometeor impact effects.

TABLE OF CONTENTS

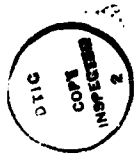

LIST OF FIGURES

LIST OF FIGURES (continued)

LIST OF FIGURES (continued)

LIST OF TABLES

INTRODUCTION

A variety of calculational, analytical and literature survey studies, results of which are reported here, were undertaken by Atmospheric Science Associates to assist the Cloud Physics Branch, Meteorology Division, Air Force Geophysics Laboratory in the design of a cloud water content meter (WCM) and a hydrometeor spectrometer (HS). Both of these instruments are to be airborne on cloud physics research airplanes. The critical measurement element of both is a flat, circular annular surface which is rotating at high speed and is oriented normal to the airplane flight path. Thus, hydrometeor impact trajectories are approximately normal to the annular surfaces. Both instruments use momentum effects of collected hydrometeors on rotation speed to measure, in the case of the WCM, cloud water content, and in the case of the HS, masses of individual hydrometeors. Rotation of the annuli is caused by flow of air against vanes, or torque blades as they are called here, which are mounted on the annuli surfaces. Figure 1 is an artist's sketch of the geometry of the WCM.

Our studies have been of three types:

1. Flow field and water drop trajectory calculations.
2. Theoretical analysis of torque on the torque blades.
3. Hydrometeor impact effects.

Details are presented in the three chapters which follow. These studies are but a fraction of the total design effort, the bulk of the work having been done in-house at the Air Force Geophysics Laboratory. The part of Atmospheric Science Associates in the overall effort was to assist in the solution of various technical problems, or answer various technical questions, as these arose during the design process.

Most of the effort has been devoted to the WCM, and the design of this instrument has progressed to a final stage. There has been time for only preliminary studies on the HS.

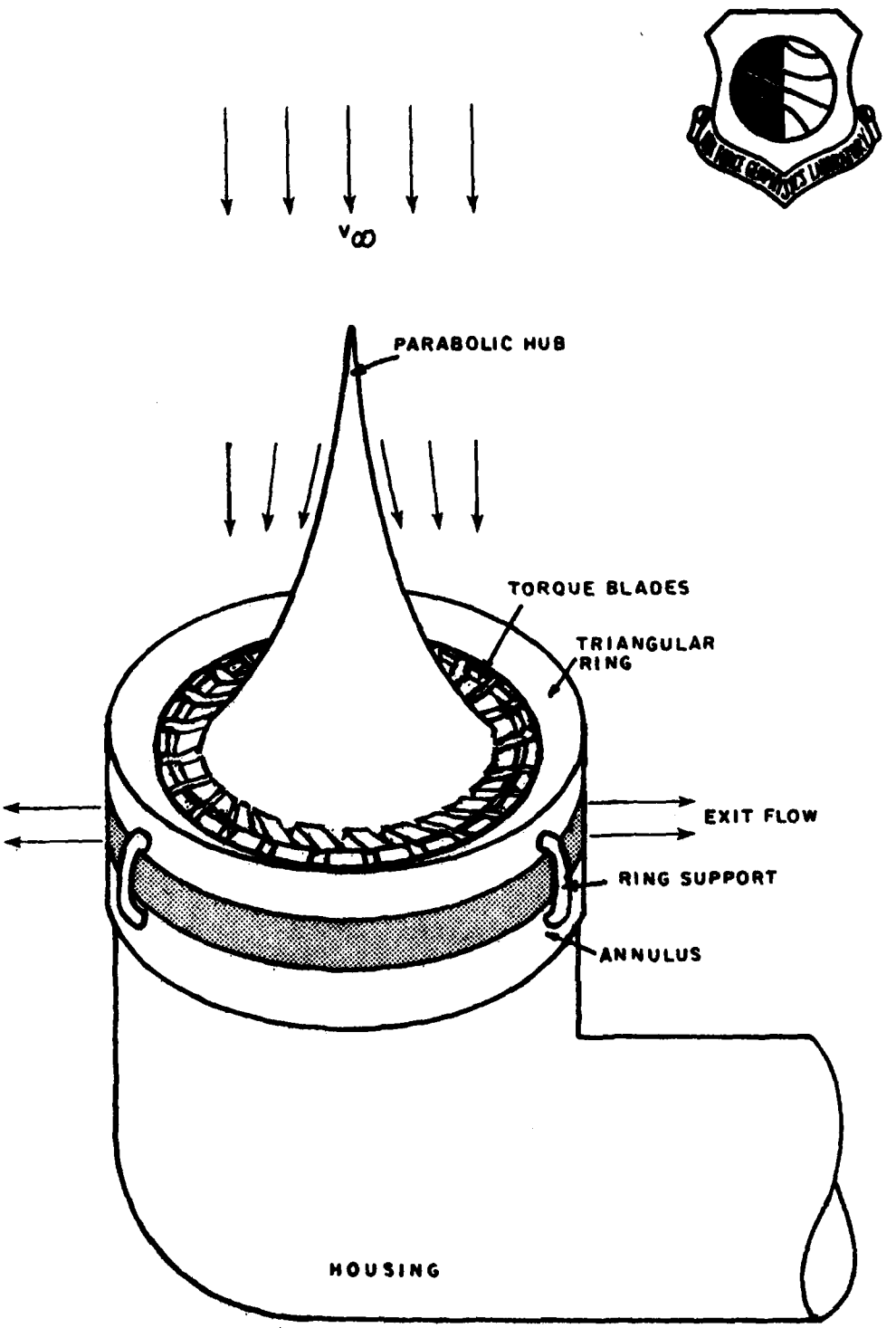

Figure 1. Artists rendition of the water content meter. (Not to proportional scale.)

FLOW FIELD AND WATER DROP TRAJECTORY CALCULATIONS

GENERAL

Flow field and trajectory calculations were performed by use of the codes developed by Norment[1]. The codes calculate potential flow in three dimensions about bodies of arbitrary shape by use of the method of Hess and Smith[2]. Trajectories of water drops of any size are calculated through the flow fields by numerical integration of the water drop equation of motion in which drag relations derived from experimental data are used. Details are given in reference 1.

Since potential flow is calculated, effects of friction are not included, and the existence of a boundary layer is simply ignored. While details of the boundary layer flow would be necessary for accurate calculation of dynamic pressure forces near the surface of the annuli and blades, the effort required would have been beyond the scope of this program. Moreover, most of the critical information required for the instrument design can be obtained without considering the details of the boundary layer flow.

To calculate flow fields about the various bodies of interest, it is necessary to develop digital descriptions of the surfaces of the bodies in terms of appropriate configurations of many small, contiguous, plane panels or elements. Computer-drawn plots of the element configurations are given below, along with the results of the flow field and trajectory calculations.

Since friction is ignored, rotation of the annuli also is ignored. This being the case, accounting for flow about the rotating blades is somewhat of a problem. In some of the calculations discussed below the blades are ignored, but for the final configuration of the WCM they are included in approximate form.

---

1. H. G. Norment, "Calculation of Water Drop Trajectories to and About Arbitrary Three-Dimensional Bodies in Potential Airflow," Atmospheric Science Associates, NASA CR 3291 (August 1980). N80-28302

2. J. L. Hess and A. M. O. Smith, "Calculation of Non-Lifting Potential Flow About Arbitrary Three-Dimensional Bodies," McDonnell Douglas Report E. S. 40622 (15 March 1962). AD-282 255

SIMPLE DISC

Figure 2 shows the digital description used to represent a simple disc collector of radius R = 3 cm. In this case, as in those to follow, the downstream housing is represented by a crudely resolved cylinder, while the collection face is sufficiently well resolved to allow for determination of the flow field near its surface.

Water drop trajectories are shown in Figures 3. Figure 3a can be considered to show flow streamlines. Impaction efficiencies, E, calculated from these trajectories are shown on the figures*. Figure 4 shows the flow field near the surface.

DISC WITH PARABOLIC HUB

The simple disc collector was modified by addition of a non-rotating, cylindrically symmetric parabolic hub, which at its extreme upwind extension ends in a needle-like point. The equation of the parabola is

$$(r/r_2 - 5/6)^2 = -\frac{1}{3}(x/r_2 - 1/12) \qquad (1)$$

where r is radial distance from the disc axis, x is distance in the direction of the free stream flow, with origin at the disc face, and r_2 is the disc radius (3 cm).

Figure 5 shows the crossection plane through the device that includes the symmetry axis. The hub intersects the face of the disc at coordinates ($x/r_2 = 0$, $r/r_2 = 2/3$), and the focus of the parabola is at point ($x/r_2 = 0$, $r/r_2 = 5/6$). The annular section of the disc surface between $r/r_2 = 2/3$ and $r/r_2 = 1$ is the collection (i.e., measurement) surface, and is rotating at high speed.

---

*Impaction efficiency is the ratio of particle flux actually incident on the collection surface to particle flux in the free stream.

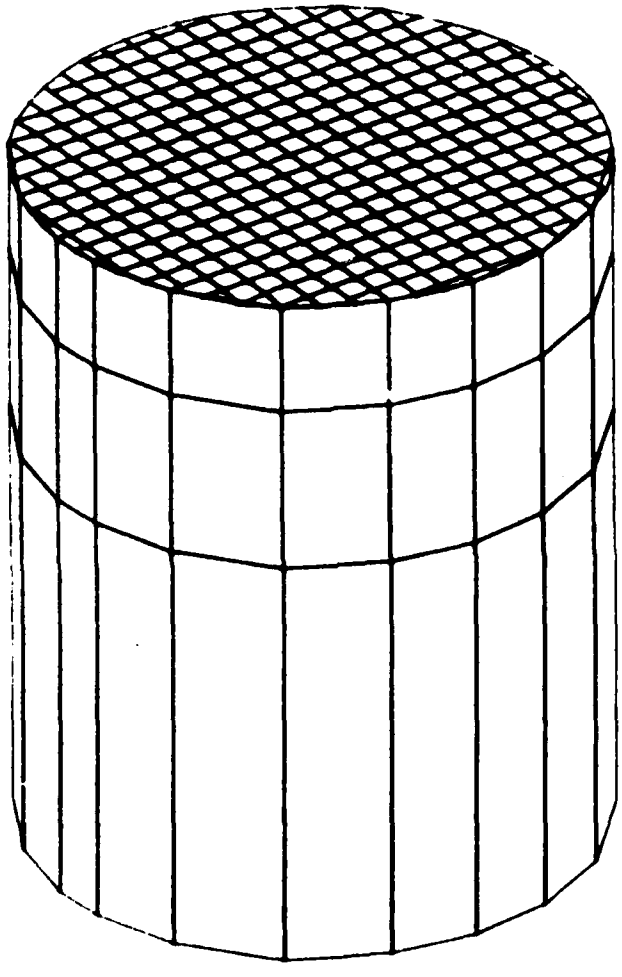

Figure 2. Digital description of a simple disc collector with housing.

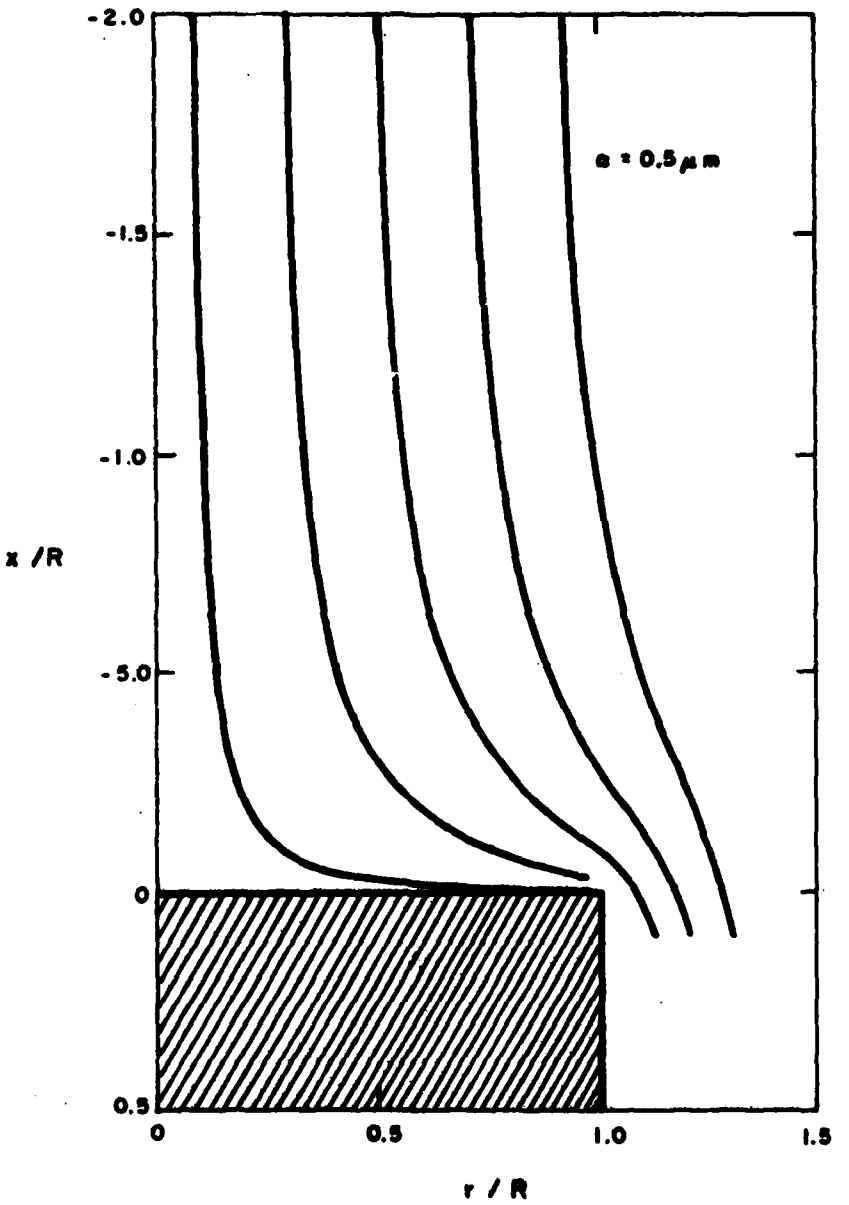

Figure 3a. Trajectories of water drops of radius 0.5 μm to the disc collector. These trajectories are essentially coincident with flow stream lines. Free stream air speed is 100 m s^{-1}. R = 3 cm.

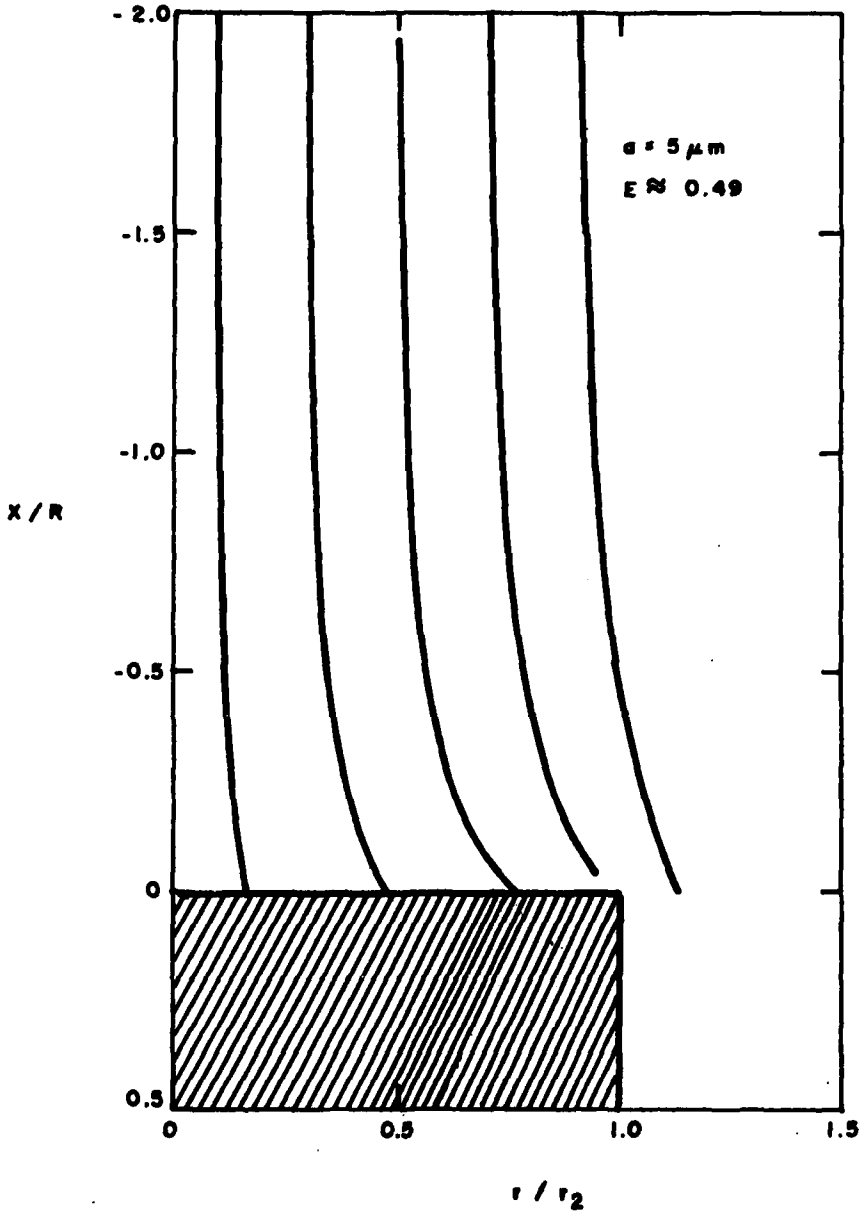

Figure 3b. Trajectories of water drops of radius 5 μm to the disc collector. E is impaction efficiency.

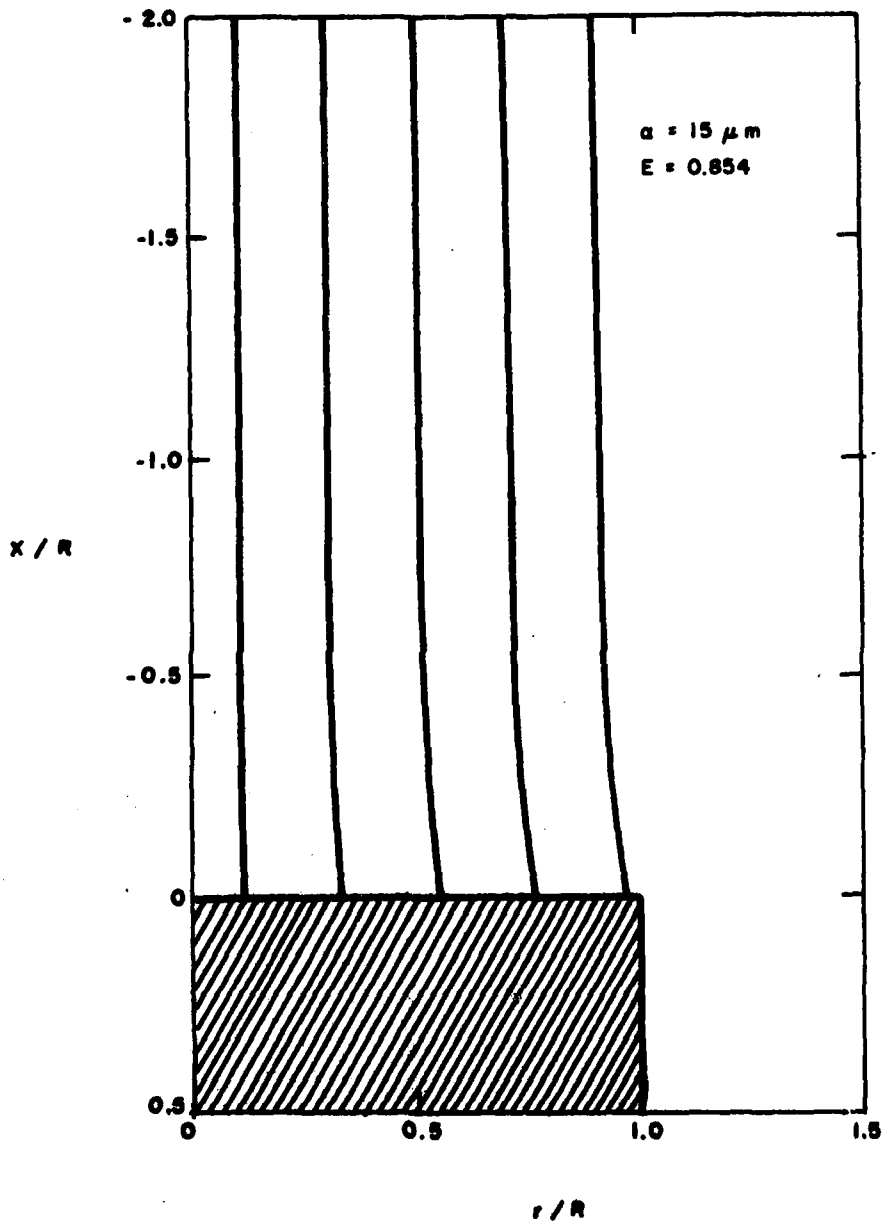

Figure 3c. Trajectories of water drops of radius 15 μm to the disc collector.

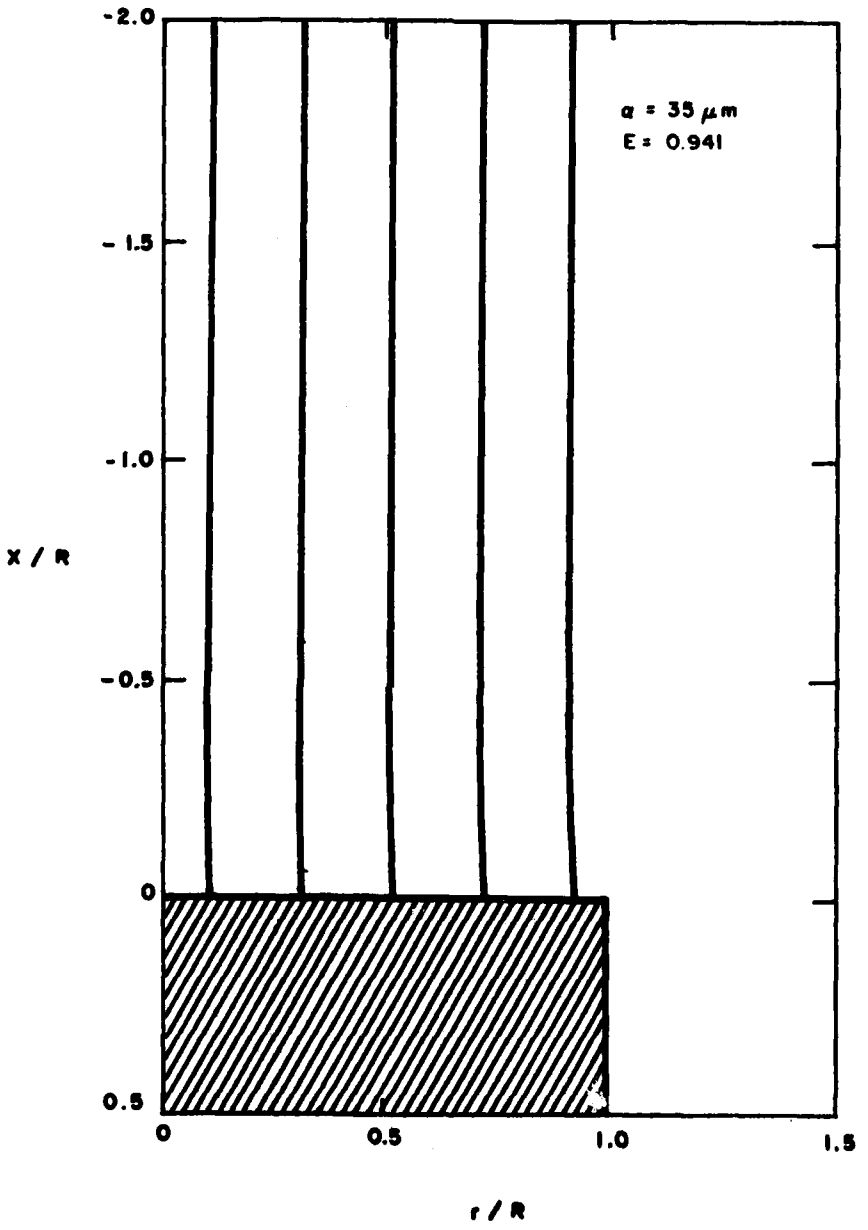

Figure 3d. Trajectories of water drops of radius 35 μm to the disc collector.

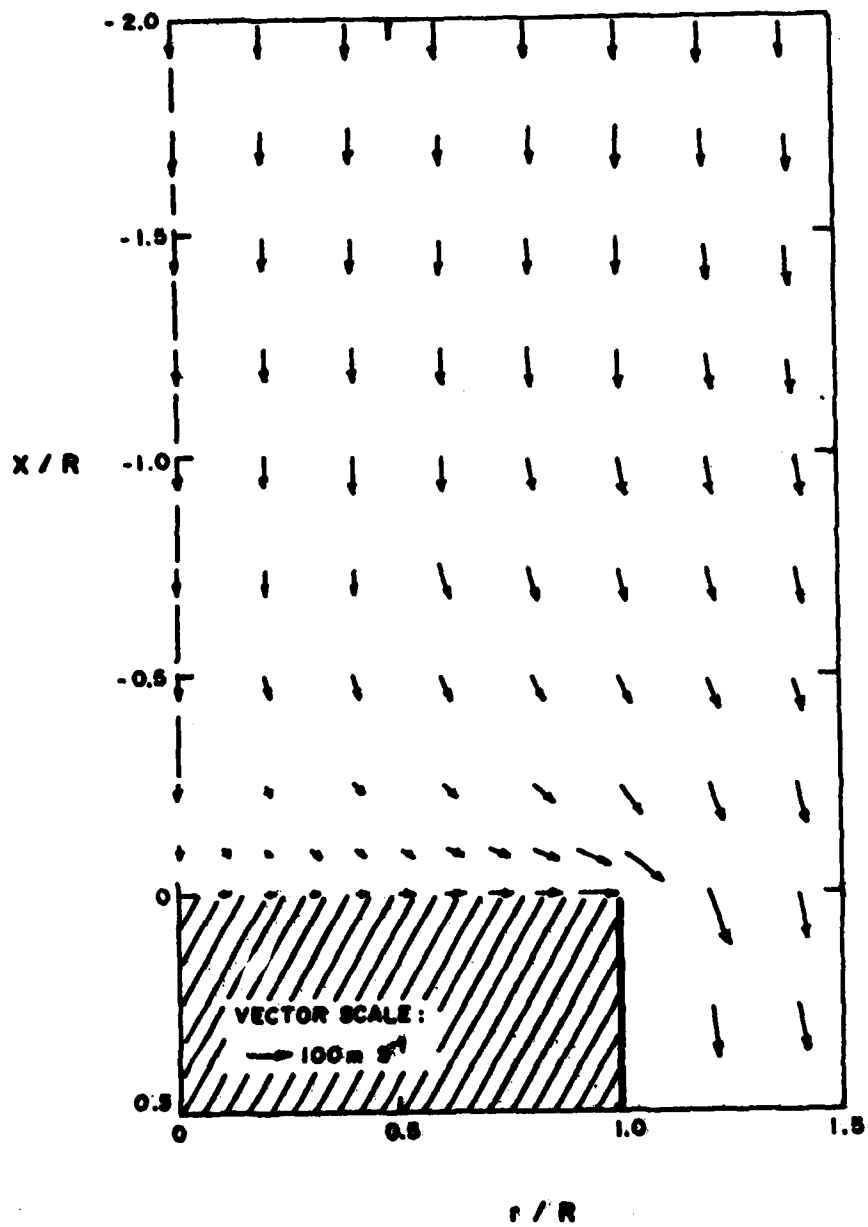

Figure 4. Flow field near the surface of the disc collector shown in Fig. 2.

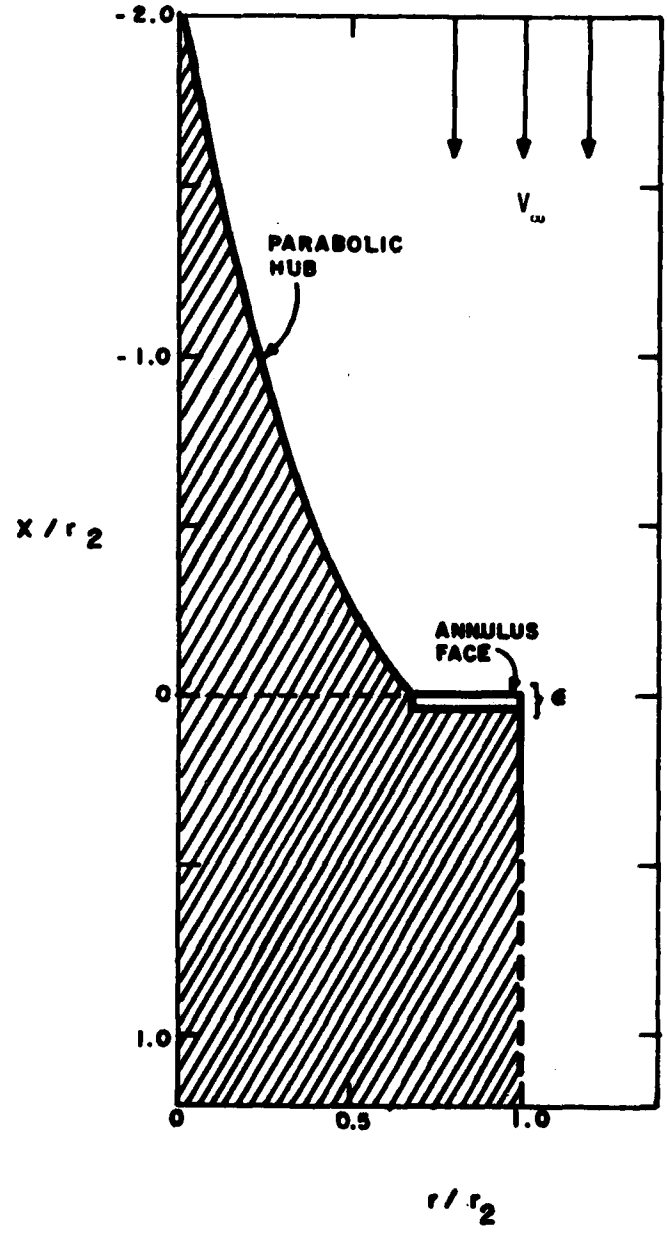

Figure 5. Crossection profile of the disc collector with parabolic hub. The x axis is a rotation symmetry axis.

Figure 6 shows the digital description used to represent this version of the WCM. Figures 7 show water drop trajectories, with those in Figure 7a being essentially coincident with flow stream lines. Impaction efficiencies, E, calculated from the trajectories are shown on the figures. Figure 8 shows the flow field close to the surface of the rotating annulus, and Figure 9 shows contours of constant radial flow component. The radial flow component near the surface of the annulus is of particular importance since the dynamic pressure of this flow acts against the blades to rotate the annulus, and to dislodge and expell hydrometeors from the annulus surface.

There are certain critical places where it is important to know the dynamic pressure on the surface of the instrument. Especially important are the gaps between rotating and nonrotating parts at which the interior of the instrument is exposed to the environment. With reference to Figure 5, such locations are the hub junction with the annulus, at point (x/r_2 = 0, r/r_2 = 2/3), and the gap between the annulus and the downstream housing, at point ($x/r_2 = \varepsilon$, $r/r_2 = 1$). At the hub junction the x component of flow is zero, and extrapolation of calculated velocities shows that the radial component also is zero. Thus, we have stagnation, and the dynamic pressure relative to ambient, ΔP_s, at this point is

$$\Delta P_s = \frac{1}{2} \rho V_\infty^2 \simeq 45.5 \text{ mb}$$

where ρ is air density and $V_\infty \simeq 100 \text{ m s}^{-1}$ is free stream air speed (i.e., the speed of the airplane).

The closest on-body point to the junction of the annulus with the housing for which we have a velocity calculation is (x/r_2 = 0.2, r/r_2 = 1.0). Here we have $v_x/V_\infty = 2.4$, $v_r/V_\infty = 0$. The pressure

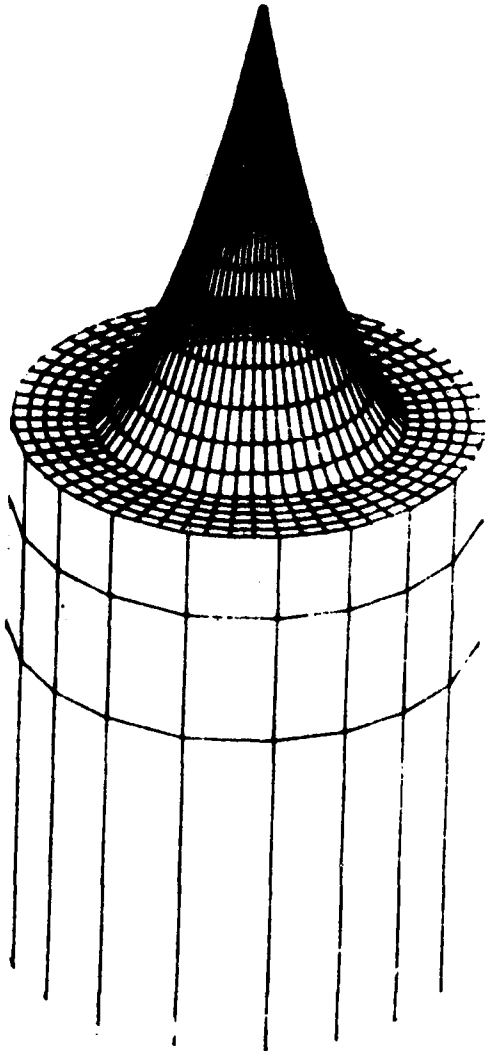

Figure 6. Digital description of the disc collector with parabolic hub.

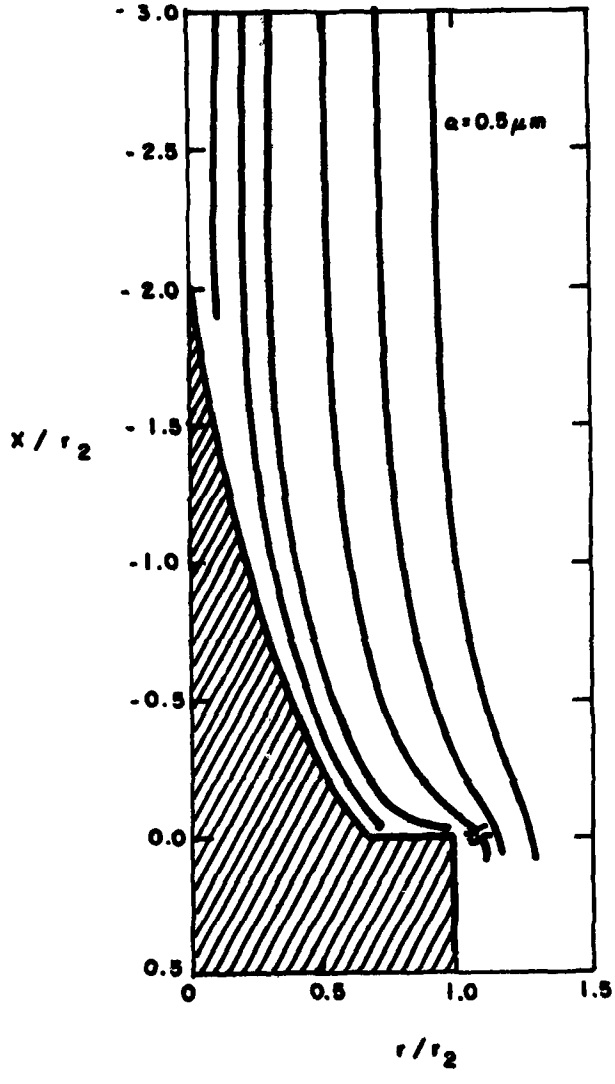

Figure 7a. Trajectories of water drops of radius 0.5 μm to the disc with parabolic hub. These trajectories are essentially coincident with flow stream lines. Free stream air speed is 100 m s^{-1}. r_2 = 3 cm.

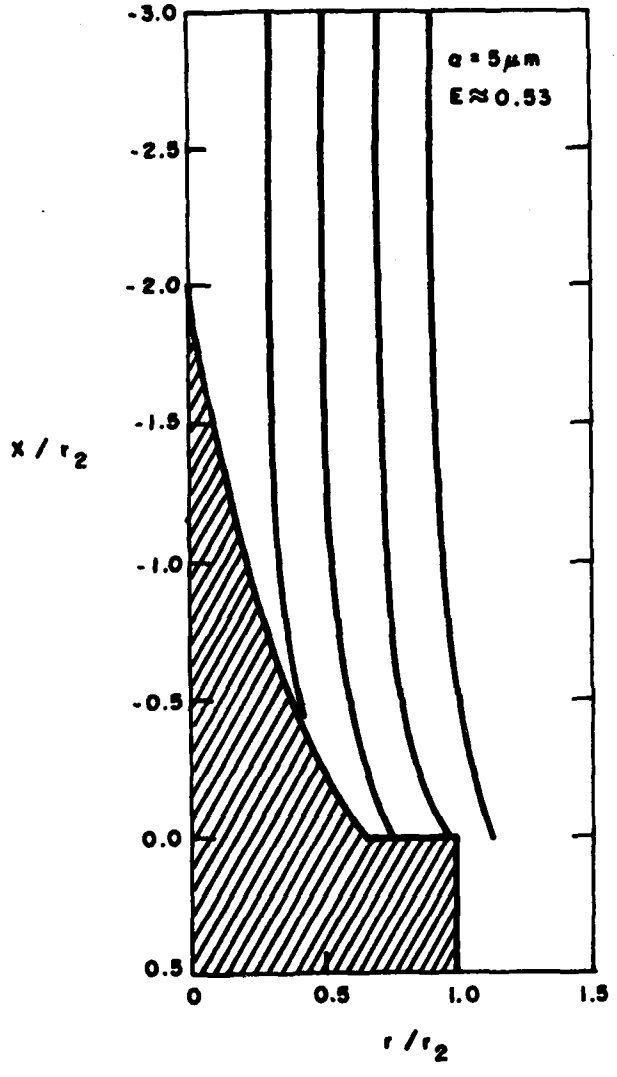

Figure 7b. Trajectories of water drops of radius 5 μm to the disc with parabolic hub. E is impaction efficiency.

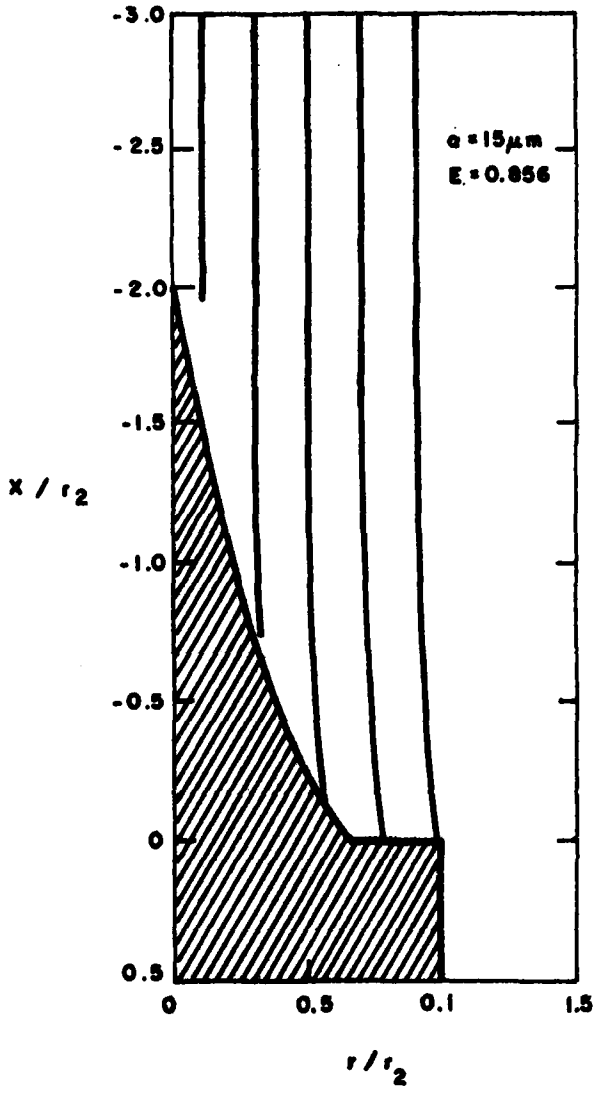

Figure 7c. Trajectories of water drops of radius 15 μm to the disc with parabolic hub.

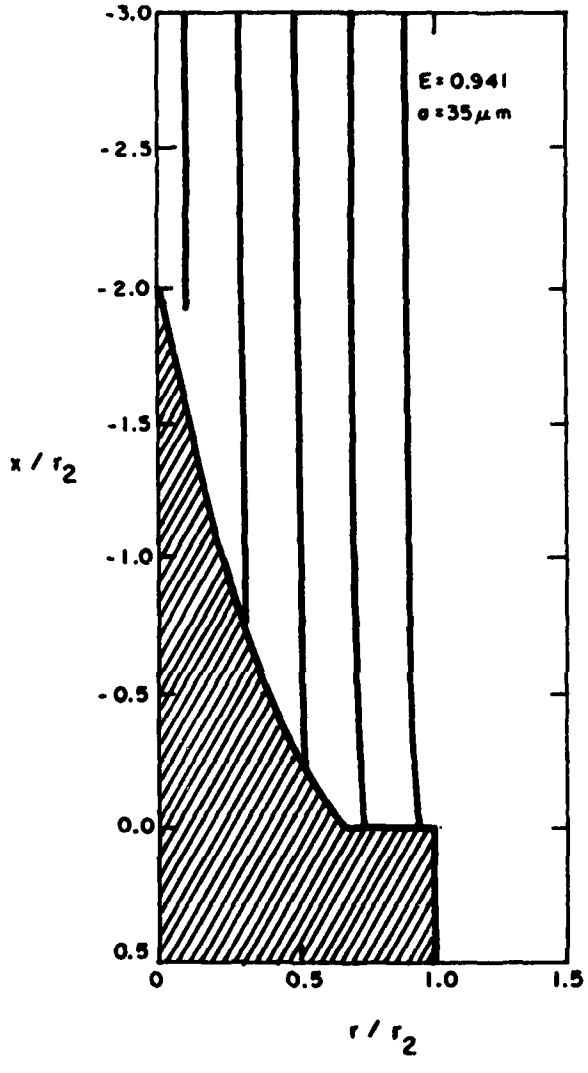

Figure 7d. Trajectories of water drops of radius 35 μm to the disc with parabolic hub.

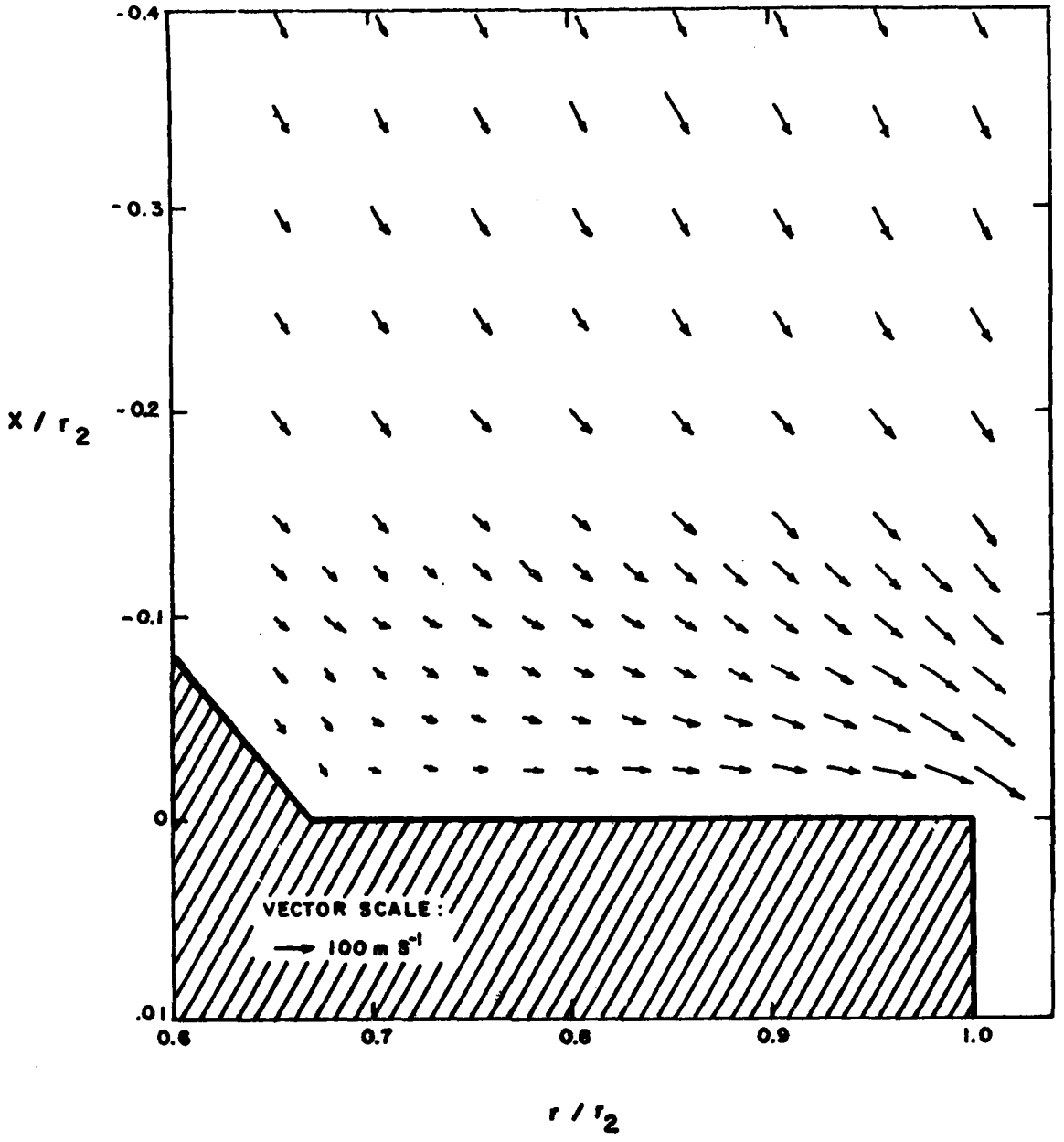

Figure 8. Flow field near the annulus surface of the disc with parabolic hub. (See Figs. 5 and 6.)

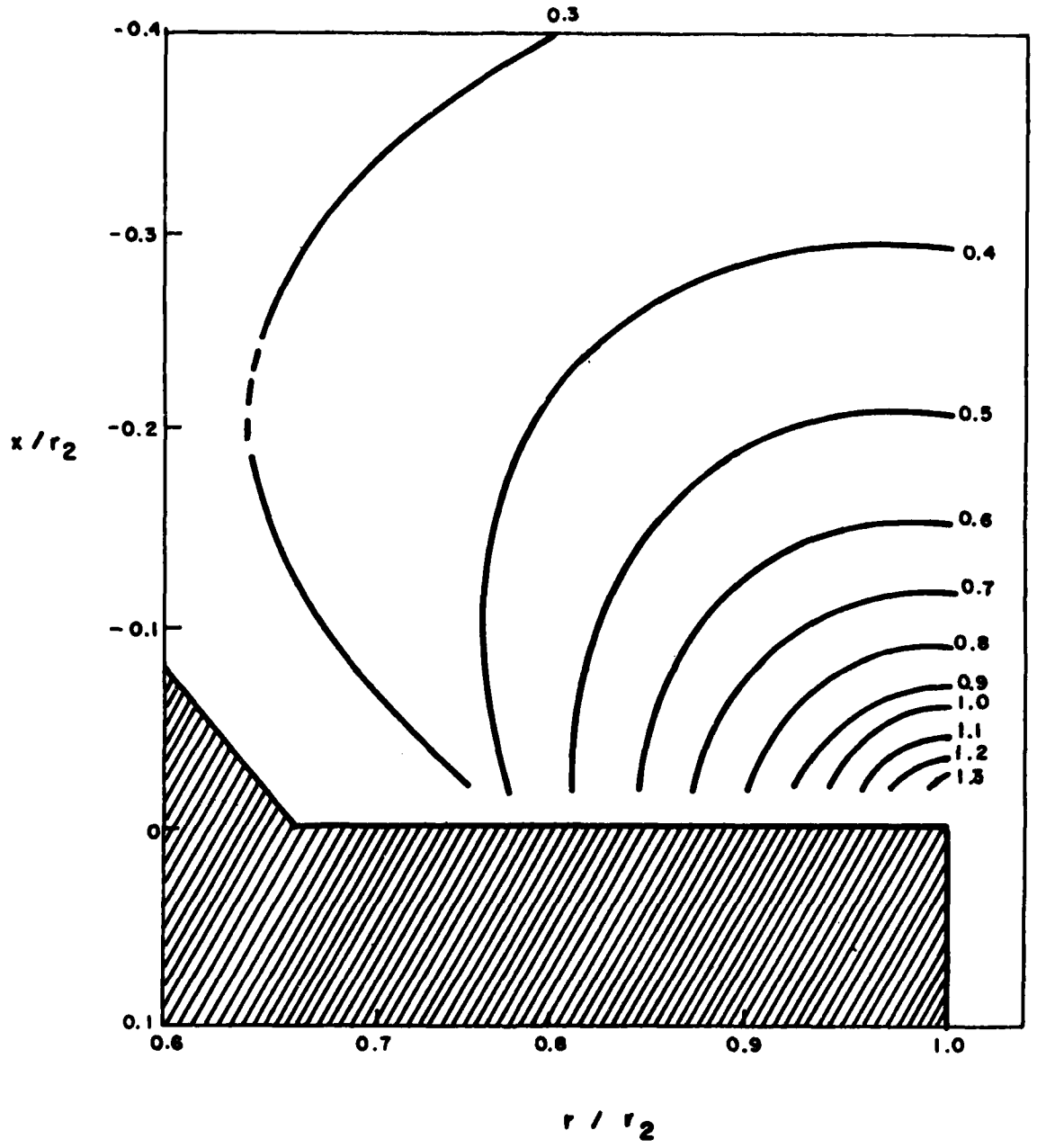

Figure 9. Contours of constant radial flow component, v_r/V_∞, near the annulus surface of the disc with parabolic hub. (See Figs. 5 and 6.)

relative to ambient is

$$\Delta P = \frac{1}{2} \rho V_\infty^2 \left[1 - (v_x/V_\infty)^2 \right] \simeq - 63.6 \text{ mb.}$$

Thus at the hub junction we have dynamic pressure acting to force water into the interior of the instrument, whereas at the housing junction we have a suction outward from the interior. These facts have been accounted for in the design of the instrument housing.

DISC WITH PARABOLIC HUB AND TRIANGULAR RING

A further modification to the WCM was made by addition of a ring with triangular crossection upstream of the outer edge of the rotating annulus as shown in Figure 10. The purpose of the ring is to supply heat to melt ice hydrometeors and to shade the outer edge of the annulus from direct impaction. As will be seen below, the ring also serves to increase, and make more nearly constant, the radial airflow component near the annulus surface.

We also consider the effect on the flow of the presence of the torque blades. As indicated in Figure 11a, the blades are positioned at 12° intervals around the annulus (there are 30 blades), and the width of each blade covers a 5° arc of the annulus circle. The center line from end-to-end of each blade is inclined at an angle of 41.5° to the radial direction, the angle being measured at the outer edge of the annulus.*

Figure 11b shows the projection of the blades in the crossection plane. In the radial range r = 2.0 to 2.5 cm the blade height is 1 mm; it then tapers upward to a height of 5 mm, which height is reached at r = 2.7 cm, and then remains constant to $r = r_2 = 3$ cm. Since the annulus

*This corresponds to angle β of Fig. 21.

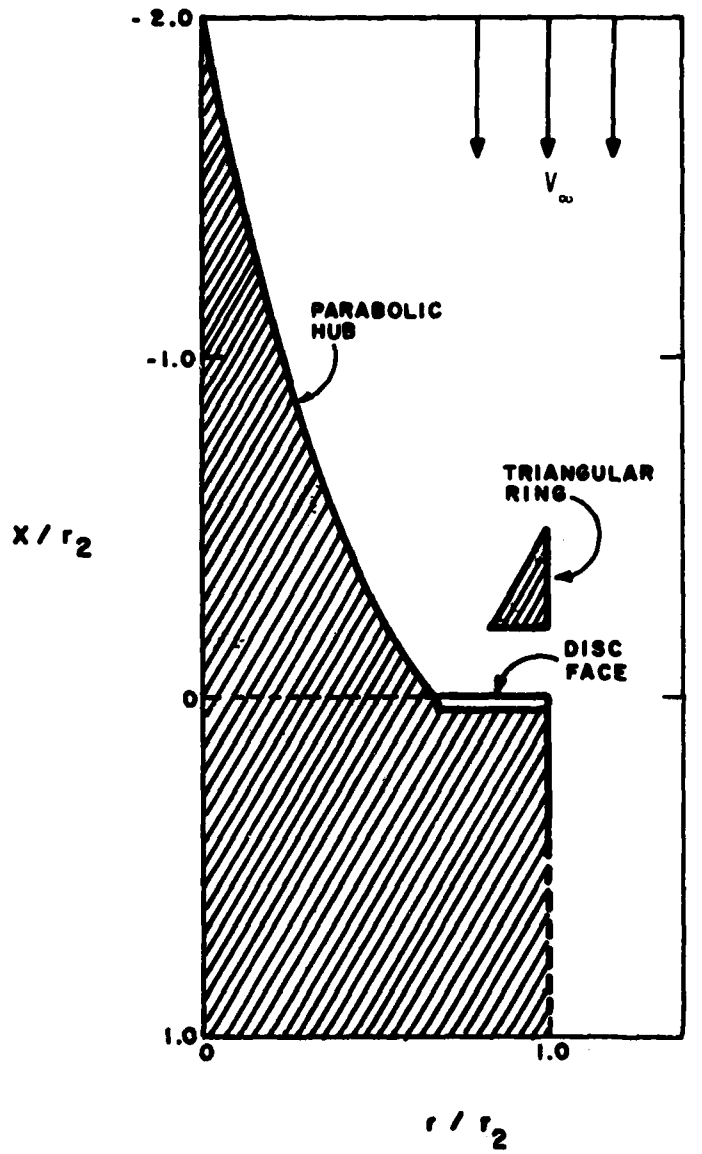

Figure 10. Crossection profile of the disc collector with parabolic hub and triangular ring. The x axis is a rotation symmetry axis.

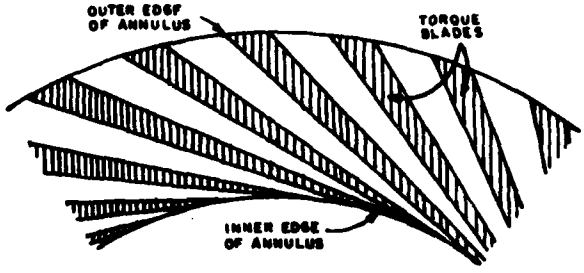

a. Plan view of the stationary annulus showing the torque blades.

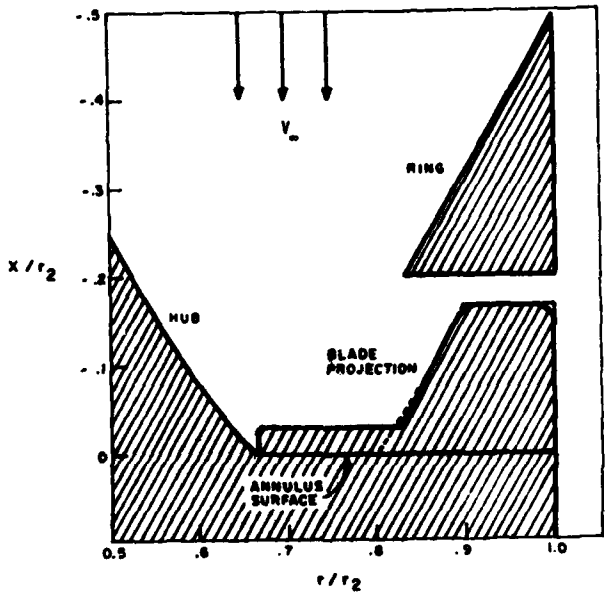

b. Crossection profile of the disc collector with parabolic hub and triangular ring showing a projection of the torque blades on the plane of the drawing.

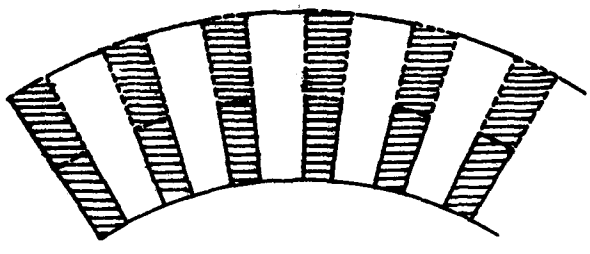

c. Plan view of the annulus showing the torque blades approximately as seen by the radial flow when the annulus is rotating at equilibrium speed.

Figure 11. Torque blade geometry for the water content meter. Drawings are to proportional scale

and blades rotate at very close to equilibrium speed, the air that passes through the blades sees a configuration approximately like that of Figure 11c. We have included the tall portion of the blades, as outlined by the broken lines in Figures 11b and 11c, in the digital description (Fig. 12).

Figures 13 and 14 show the flow field and radial component of flow near the surface of the annulus. The plane of the calculation is midway between two torque blades. The presence of the ring and blades is seen to increase the radial flow speed and make it more nearly constant in the x axis direction (cf. Fig. 9).

Figure 15 shows the variation of radial flow component with r/r_2 close to the surface of the annulus ($x/r_2 = -0.02$). Note that the curve is approximately linear out to $r/r_2 \approx 0.85$.

(A similar calculation for a smaller triangular ring and slightly different blade geometry also was calculated, but that design was supplanted by the one described above, and its description would add nothing of value here.)

HYDROMETEOR SPECTROMETER

At the time of this writing the hydrometeor spectrometer (HS) is in a preliminary stage of development, and the geometry discussed here is tentative. Similar to the WCM, the measurement surface of the HS is a rotating annulus that is oriented normal to the free stream flow. However, instead of having a stationary hub, the central portion of the HS is open such that flow is allowed through it. A thin wall, called the "flow splitter", rises normal to the annulus surface around its inner edge. Thus, we have stagnation at the inner edge of the annulus.

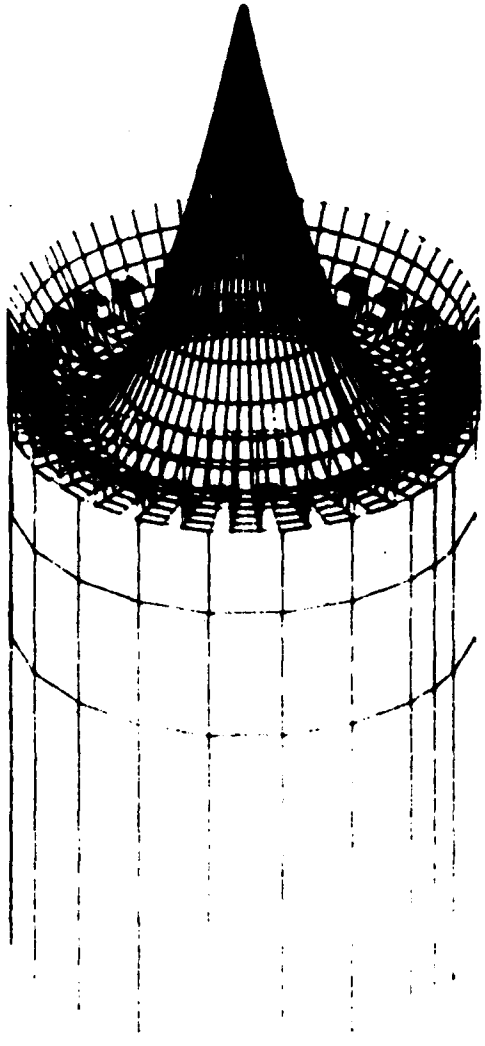

Figure 12. Digital description of the WCM with parabolic hub, triangular ring and torque blades.

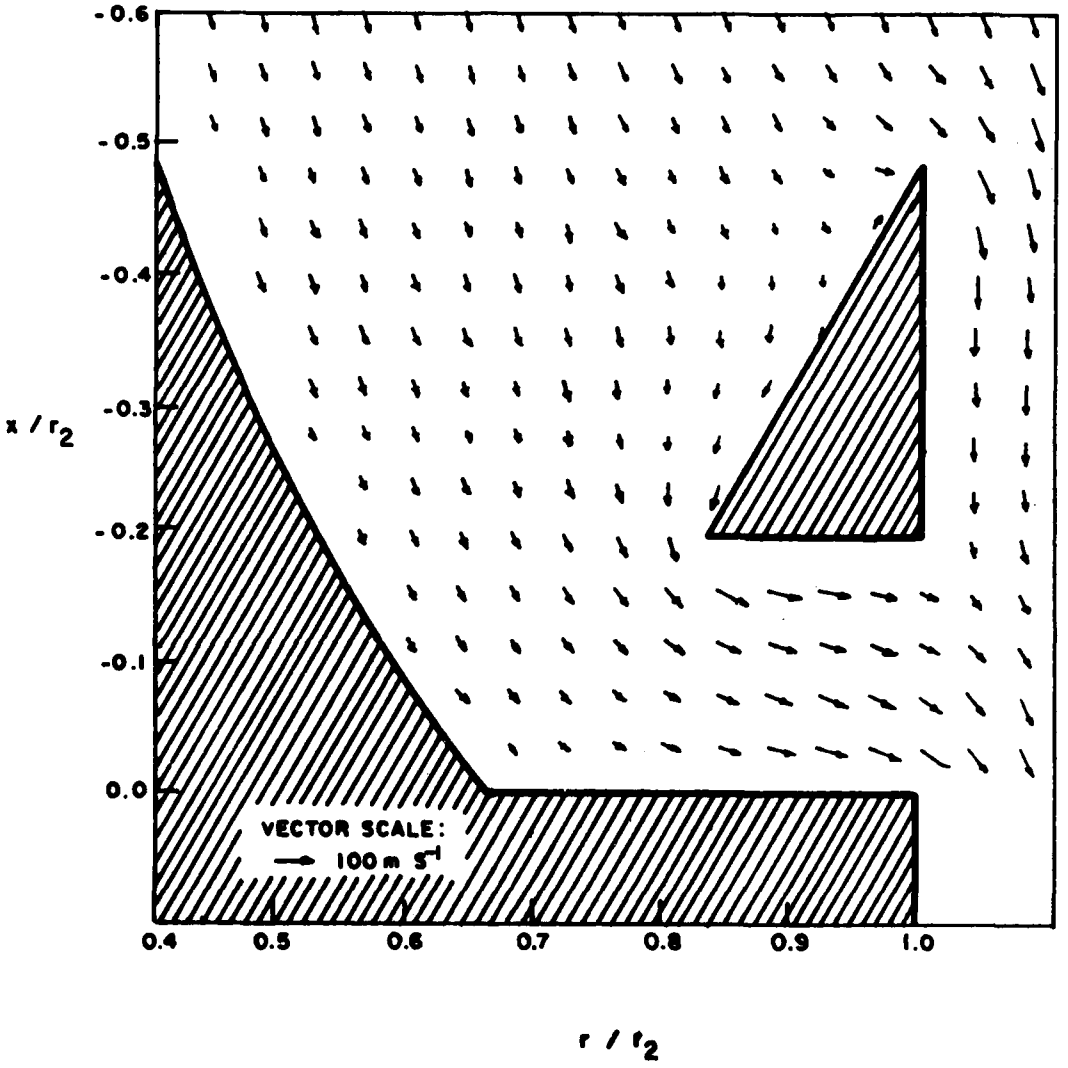

Figure 13. Flow field near the annulus surface of the WCM with parabolic hub, triangular ring and torque blades. The plane of the calculation is midway between two torque blades.

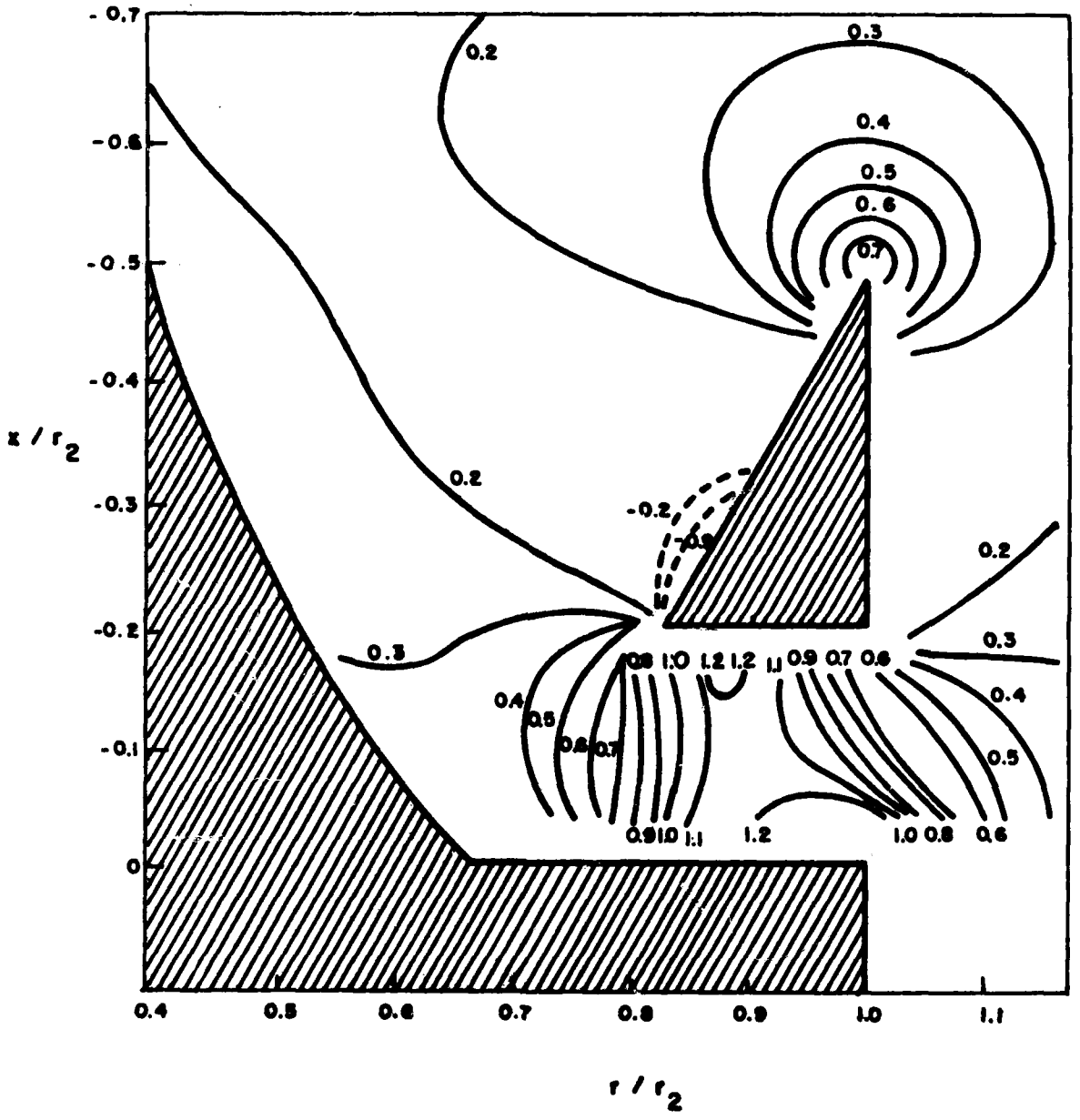

Figure 14. Contours of constant radial flow component, v_r/V_∞, near the annulus surface of the WCM with parabolic hub, triangular ring and torque blades. The calculation plane is midway between two torque blades.

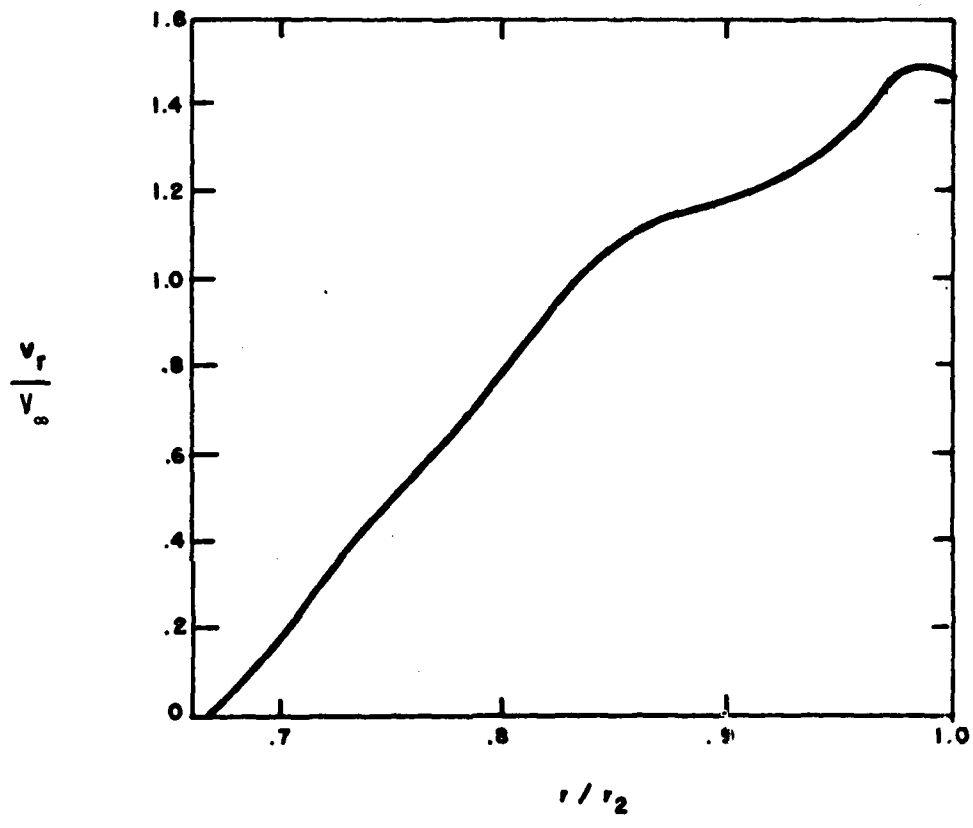

Figure 15. Radial flow component at distance $x/r_2 = -0.02$ from the surface of the WCM annulus.

Inner and outer radii of the annulus are, respectively, r_1 = 5 cm and r_2 = 7 cm. To obtain a crude approximation to the flow field near the surface of the annulus, the geometry shown in Figure 16 was used to develop a digital description of the annulus. The flow splitter is not actually included in the geometry; instead, the inner edge of the annulus is extended inward from r/r_2 = 0.714 to 0.5. The value 0.5 was chosen because we estimated that the stagnation point on an annulus surface of these dimensions should be near the desired value of r/r_2 = 0.714. Figure 17 shows the digital description used.

Figures 18 and 19 show the flow field near the annulus surface and contours of the radial component of flow. Stagnation occurs at $r/r_2 \approx$ 0.64 instead of 0.714, and the zero contour bends toward the symmetry axis instead of rising vertically from the annulus surface as it should for an accurate modeling of the flow splitter surface. Nevertheless, these figures provide a qualitative picture of the expected flow.

Figure 20 shows the variation of the radial component of flow very close to the annulus surface (x/r_2 = -0.02) with r/r_2. The curve is approximately linear out to $r/r_2 \approx 0.9$.

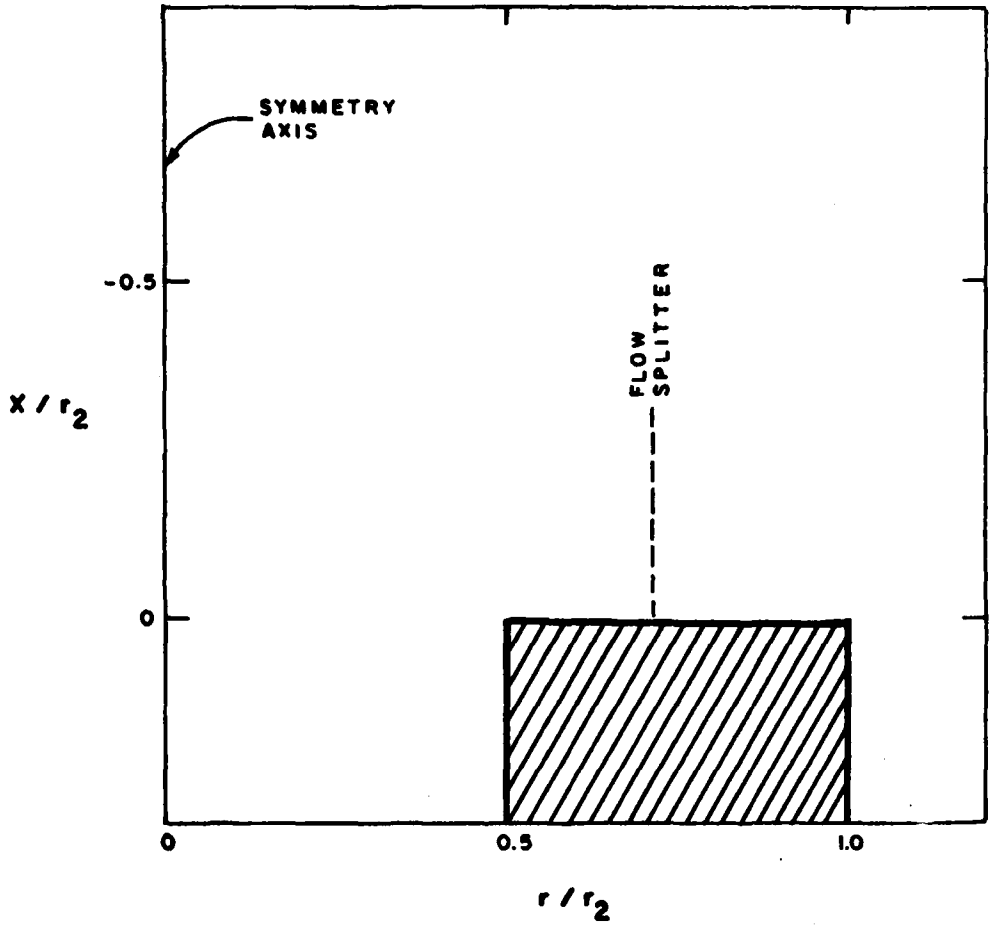

Figure 16. Geometry used for the hydrometeor spectrometer annulus digital description. The x axis is a rotation symmetry axis. The flow splitter is not actually included in the digital description.

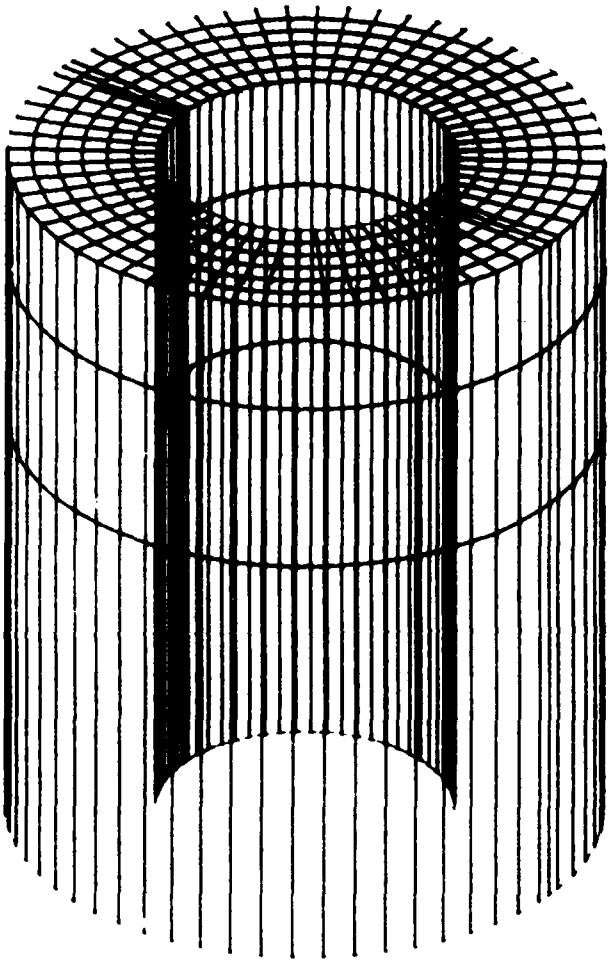

Figure 17. Digital description used to approximate the hydrometeor spectrometer annulus and housing.

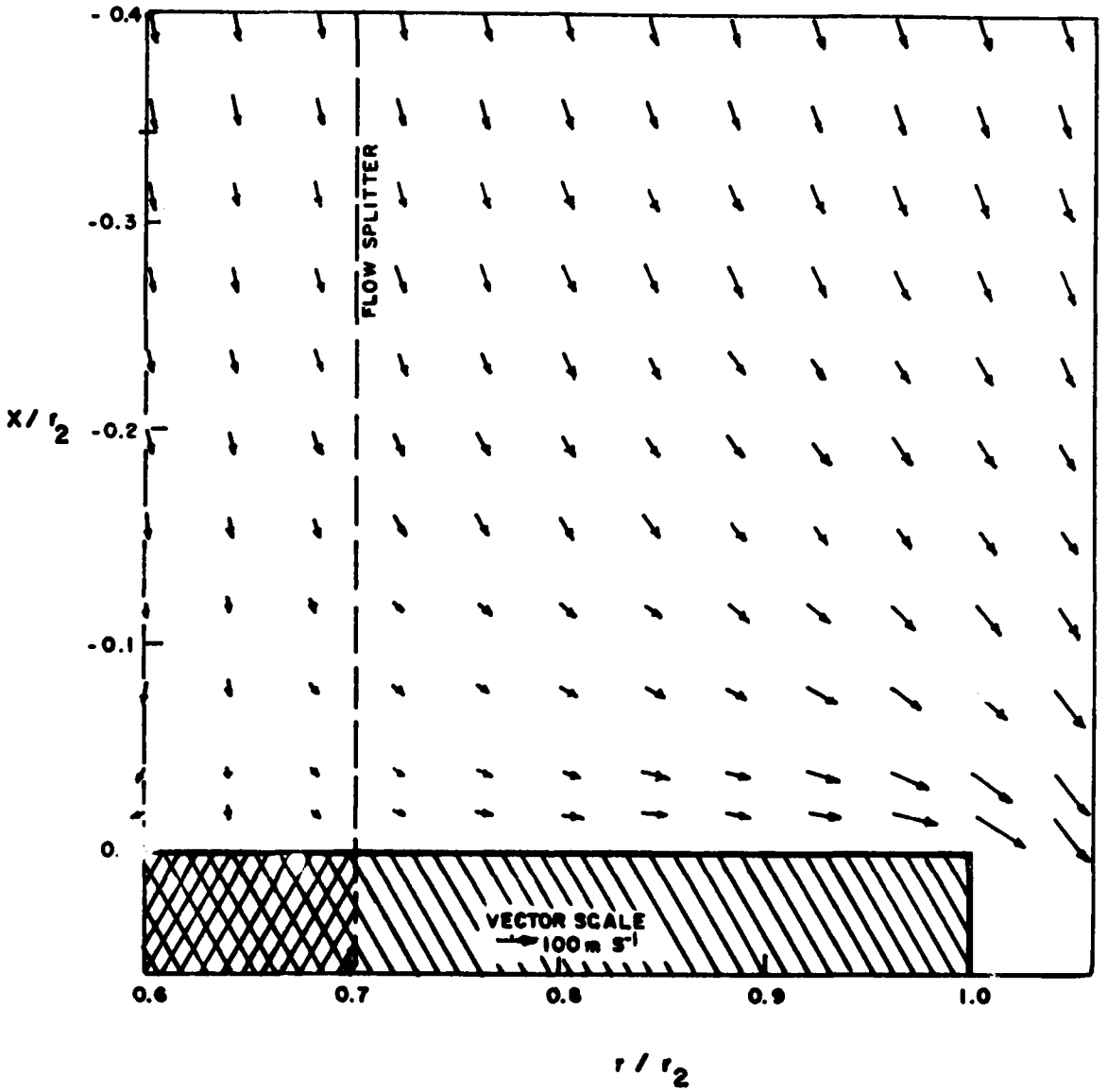

Figure 18. Flow field near the annulus surface of the annular cylinder shown in Figs. 16 and 17.

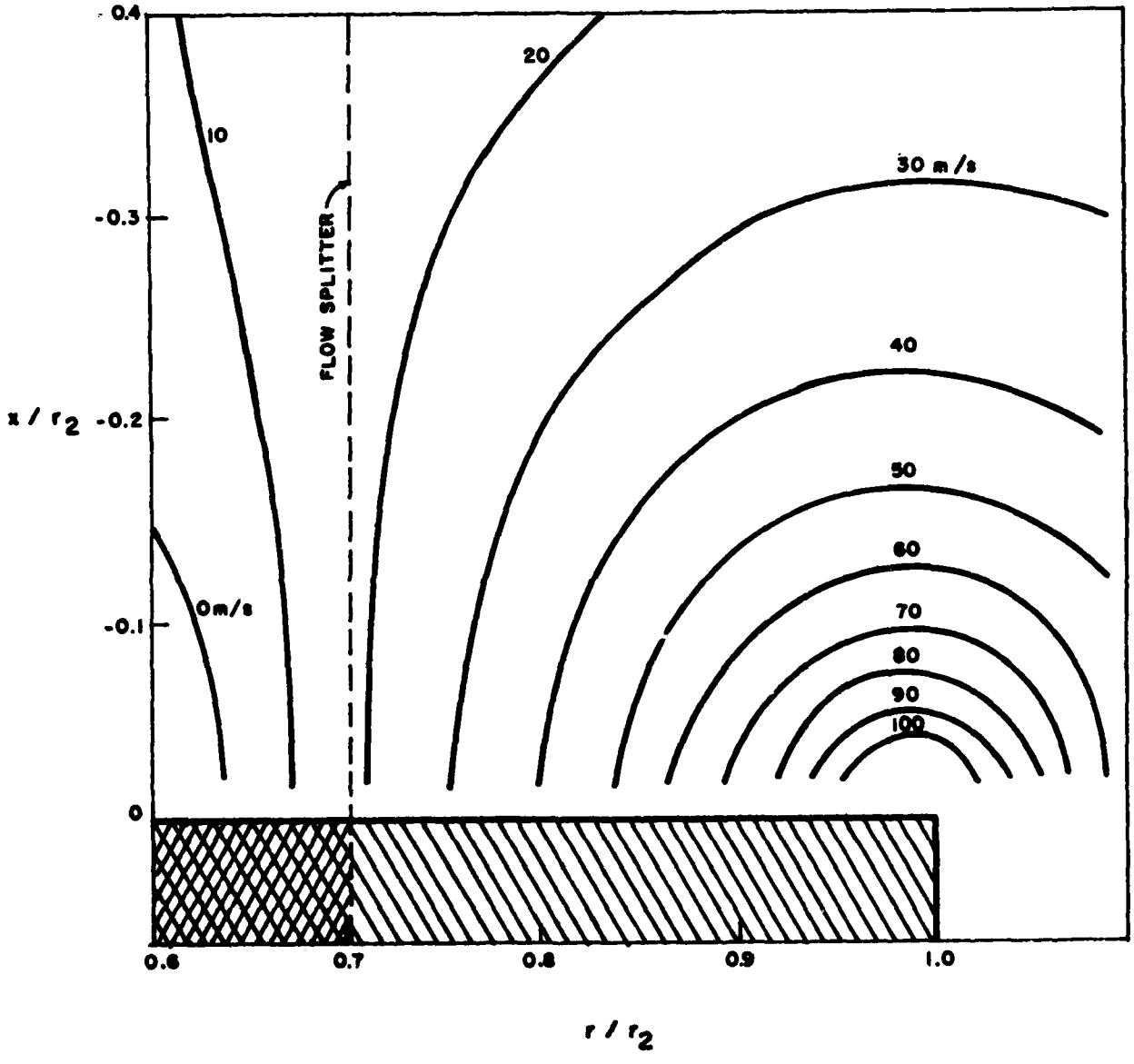

Figure 19. Contours of constant radial flow component, v_r, near the annulus surface of the annular cylinder shown in Figs. 16 and 17.

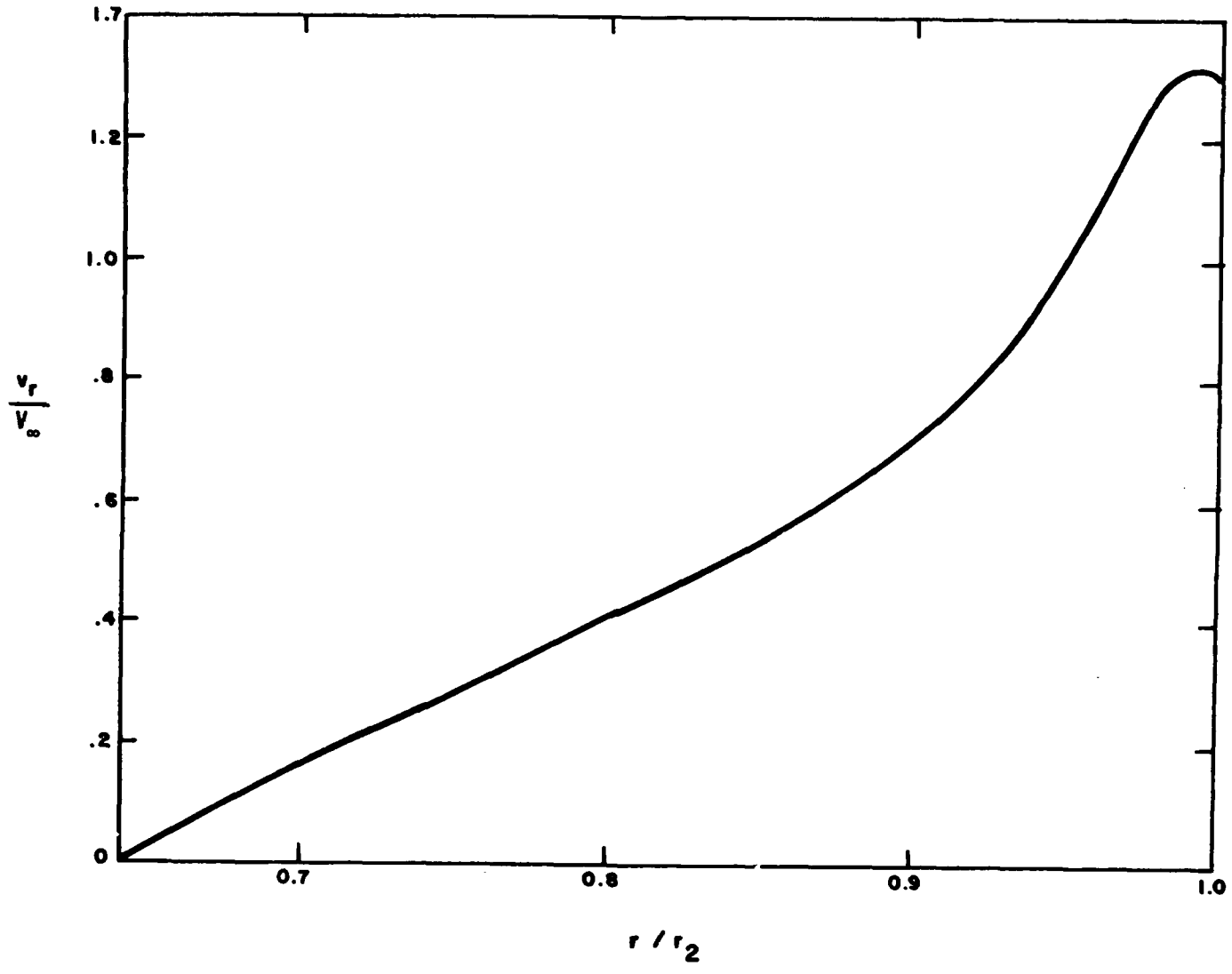

Figure 20. Radial flow component at distance $x/r_2 = -0.02$ from the annulus surface of the annular cylinder shown in Figs. 16 and 17.

CALCULATION OF TORQUE ON THE TORQUE BLADES

OUTLINE OF THE ANALYSIS

The annuli of both the water content meter (WCM) and hydrometeor spectrometer (HS) are driven rotationally by vanes, called torque blades, that are mounted at an angle to the radial flow across the annular surfaces as shown in Figure 11 for the WCM. Here we simplify the geometry to an annulus with a single blade. As shown in Figure 21, the blade is mounted at an angle to the flow such as to cause clockwise rotation of the annulus at angular speed ω.

In our analytical treatment we make the following restrictions and approximations:

1. The blade is thin, straight and of constant height, h.
2. Radial air speed across the annulus, v_r, is constant with distance from the surface in the negative x axis direction.
3. v_r is either constant with r, or increases linearly with r beginning at $v_r = 0$ at $r = r_1$. (See Fig. 21 for notation.)
4. The annulus is rotating at or near to its equilibrium speed, and the blade offers negligible obstruction to the flow.

While none of these assumptions are in accord with actuality, the last is probably the most unsatisfactory from a theoretical point of view. This is because, as indicated in Figure 21, the angle α between the radial direction and the blade varies across the length of the blade, and, as we shall see below, even at equilibrium there is a distribution of nonzero dynamic pressures across the blade. Consequently, there will be a reaction on the air which must distort its flow.

The remainder of the restrictions can be relaxed, and more exact calculations can be done, if numerical rather than analytical integration methods are used.

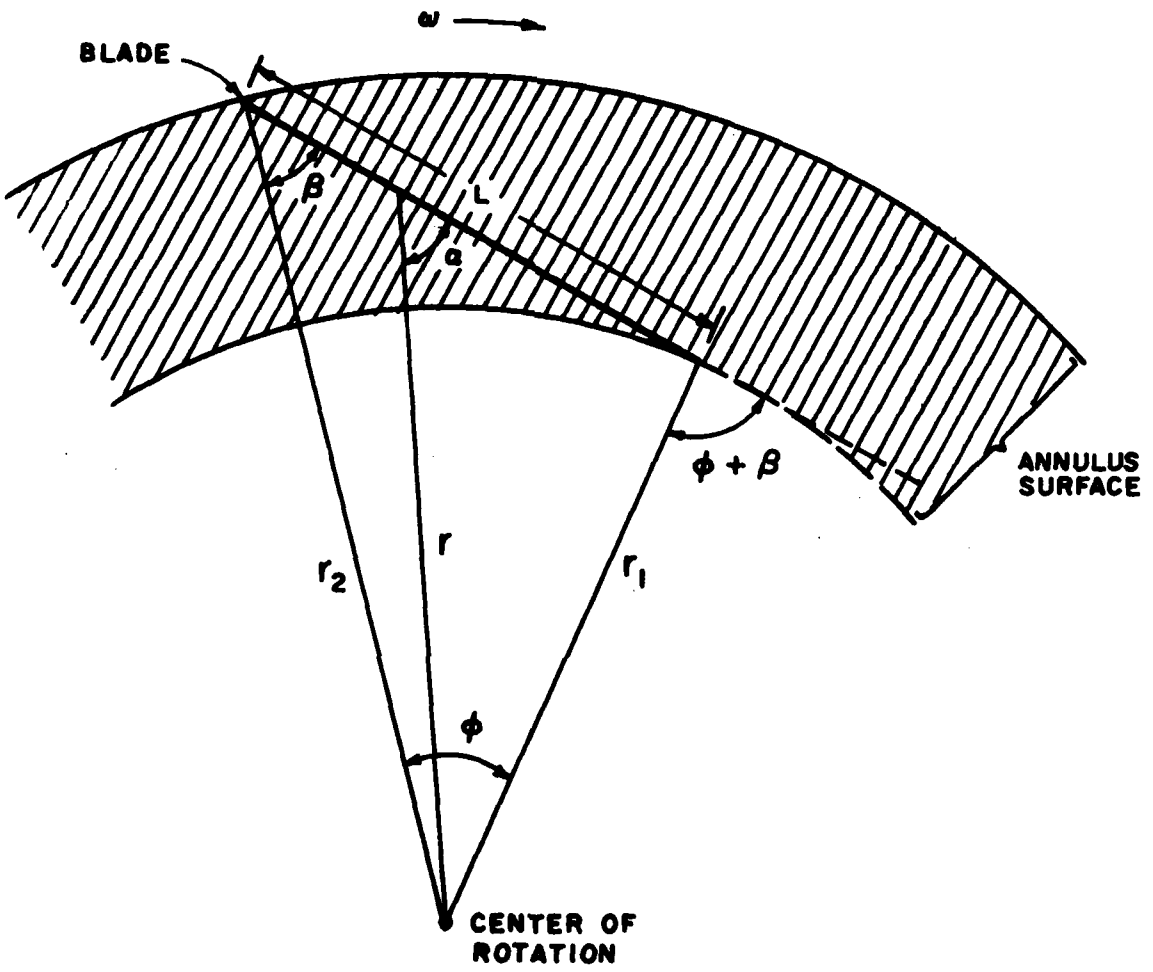

Figure 21. Plan view of a disc annulus with a single torque blade. Basic parameters used in the torque analysis are defined.

DIFFERENTIAL TORQUE

We begin by computing the dynamic pressure exerted on the blade at a radial distance r from the center of rotation. At this point, the radial axis makes an angle α with the blade. The blade (and annulus) are rotating at speed ω.

From Figure 22, we see that in a frame of reference on the rotating blade, air flow vector is $\vec{v}$, and the component of $\vec{v}$ normal to the surface of the blade is $\vec{v}_p$. Therefore, the dynamic pressure on the blade, ΔP, is

$$\Delta P = \tfrac{1}{2} \rho \vec{v}_p^{\,2} \quad . \tag{2}$$

It is easy to show from Figure 22 that

$$\vec{v}_p = s(-\vec{i} \cos \alpha + \vec{j} \sin \alpha) \tag{3}$$

where

$$s = v_r \sin \alpha - \omega r \cos \alpha \tag{4}$$

and $\vec{i}$ and $\vec{j}$ are unit vectors in the directions of the $-\vec{\omega} \times \vec{r}$ and $\vec{r}$ axes.

Consider an element of blade area of differential length dL and height h centered at our point of interest. The differential pressure force on this element of area is

$$d\vec{F} = \tfrac{1}{2} \rho \, h |\vec{v}_p| \vec{v}_p \, dL \quad . \tag{5}$$

(The use of $|\vec{v}_p| \vec{v}_p$ instead of $\vec{v}_p^{\,2}$ ensures that $d\vec{F}$ has the proper direction.) The differential torque, $d\vec{T}$, on the blade is

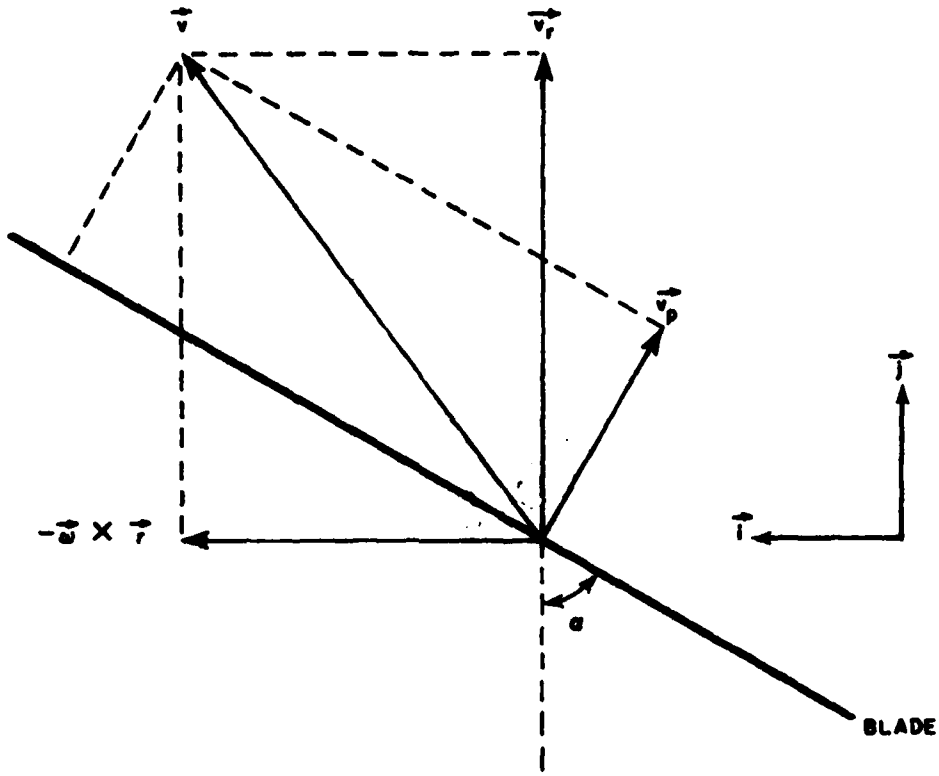

Figure 22. Vector diagram that shows the relationship of the radial flow vector, $\vec{v}_r$, the flow vector from the perspective of the rotating annulus, $\vec{v}$, and the flow component normal to the blade surface, $\vec{v}_p$.

$$d\vec{T} = \vec{r} \times d\vec{F} \tag{6}$$

where $\vec{r} = \vec{j}r$, and substitution of eqs. (3) and (5) into (6) gives

$$d\vec{T} = \vec{k}\, \tfrac{1}{2}\, \rho h r \cos\alpha |s|\, s\, dL$$

where $\vec{k}$ is the unit vector normal to the plane of Figure 22. It is convenient at this point to drop the vector notation and express r and dL in terms of α. To this purpose we use the law of sines to derive the relation (see Fig. 21)

$$r = r_2 \sin\beta \csc\alpha \tag{7}$$

from which we immediately obtain

$$r_1 \sin(\phi + \beta) = r_2 \sin\beta \quad . \tag{8}$$

Also, it is easy to prove that

$$dL = -r_2 \sin\beta \csc^2\alpha\, d\alpha \quad , \tag{9}$$

and from this we obtain

$$dT = -\tfrac{1}{2}\, \rho h r_2^2 \sin^2\beta |s|\, s\, \frac{\cos\alpha}{\sin^3\alpha}\, d\alpha \tag{10}$$

which is our basic differential torque equation in dimensional form.

To express the differential torque equation in nondimensional form, we define a nondimensional rotation speed,

$$\Omega = \omega r_2 / v_r \tag{11}$$

where ω is rotation speed with dimensions radians-time $^{-1}$,

a nondimensional $s(\alpha)$,

$$S(\alpha) = \sin\alpha - \Omega \sin\beta \operatorname{ctn}\alpha \tag{12}$$

and a nondimensional torque,

$$T = T/(\tfrac{1}{2}\rho h v_r^2 r_2^2) \tag{13}$$

where T is torque with dimensions force-length,
in terms of which eq. (10) becomes

$$dT = -\sin^2\beta |S(\alpha)| S(\alpha) \cos\alpha \csc^3\alpha \, d\alpha, \tag{14}$$

which is our basic, nondimensionalized differential torque equation.

It is apparent that the sign of the differential torque depends on the sign of $S(\alpha)$. Specifically, if $S(\alpha) > 0$ the torque boosts rotation, whereas if $S(\alpha) < 0$ the converse is true. At equilibrium or near equilibrium rotation speed, there will be a point along the length of the blade at which $S(\alpha)$ is zero; let this point be characterized by the angle α_o.

To determine total torque on the blade, eq. (14) must be integrated from $\alpha = \beta + \phi$ to β as implied by Figure 21. For actual flows and blade geometries, this would have to be done numerically. Nevertheless, it is worthwhile to study two simple cases for which the integration can be done analytically. First we consider the case with v_r constant, and then we consider linear variation of v_r with r. In both cases we take h to be constant.

TOTAL TORQUE WITH CONSTANT RADIAL FLOW

With both v_r and h constant eq. (14) can be expressed in the form

$$dT = \sin^2\beta \, \mathrm{ctn}\alpha \, (1 - \Omega \sin\beta \, \mathrm{ctn}\alpha \, \csc\alpha)^2 d\alpha \tag{15}$$

and we obtain the indefinite integral

$$\begin{aligned}\gamma(\alpha,\Omega,\beta) &= \int |dT| \\ &= \sin^2\beta \left\{ \ell n(\sin\alpha) + \Omega \sin\beta \left[\mathrm{ctn}\alpha \, \csc\alpha + \ell n(\tan\tfrac{\alpha}{2}) \right] \right. \\ &\quad \left. - (\tfrac{1}{2}\Omega \sin\beta \, \mathrm{ctn}^2\alpha)^2 \right\}\end{aligned} \tag{16}$$

As noted above, dT changes sign at $\alpha = \alpha_o$. Therefore, we must determine if α_o lies in the range $\phi + \beta$ to β, and if so, the integration of equation (15) must be done in two parts: from $\alpha = \phi + \beta$ to α_o, and from α_o to β, with the appropriate sign being taken for each part. Accordingly, we have the following situations:

1. If $\frac{S(\phi + \beta)}{S(\beta)} < 0$, we calculate α_o from the equation

$$\alpha_o = \tan^{-1} \sqrt{2 \Big/ \left(\sqrt{1 + (2/\Omega \sin\beta)^2} - 1 \right)} \tag{17}$$

and calculate the total torque from

$$T = \gamma(\beta,\Omega,\beta) + \gamma(\phi + \beta,\Omega,\beta) - 2\gamma(\alpha_o,\Omega,\beta) \tag{18}$$

2. If $\frac{S(\phi + \beta)}{S(\beta)} > 0$, we calculate the total torque from

$$T = \gamma(\phi + \beta,\Omega,\beta) - \gamma(\beta,\Omega,\beta) \tag{19}$$

but change the sign of the result if $S(\beta) < 0$.

For given geometry there is an equilibrium rotation speed, Ω_e, at which there is zero torque on the blade. We have calculated Ω_e as a function of β for the WCM geometry (i.e., r_1 = 2 cm, r_2 = 3 cm) by Newton-Raphson iteration as explained in Appendix B, and the result is plotted in Figure 23. Notice that β is limited to the range

$$0 \leq \beta \leq \beta_{max} \tag{20}$$

where from eq. (7) and Figure 21 we see that

$$\beta_{max} = \sin^{-1}\left(\frac{r_1}{r_2} \sin 90^\circ\right) \tag{21}$$

For the WCM geometry we have $\beta_{max} = 41.81^\circ$, and from Figure 23 we have $\Omega_e = 1.6915$ which corresponds to $\omega_e = 4511$ rad s^{-1} (4.307 X 10^4 RPM) for $v_r = 80$ m s^{-1}. (See Fig. 15.)

Figure 24 shows $\mathbf{T}$ vs Ω for $\beta = 33.094^\circ$ ($\phi + \beta = 54.987^\circ$) and $\Omega_e = 1.044$. Taking $v_r = 80$ m s^{-1}, this latter corresponds to $\omega_e = 2784$ rad s^{-1} (2.658 X 10^4 RPM).

Also of interest is the distribution of dynamic flow pressure across the length of the blade. For this we define a dimensionless dynamic pressure (see eq. (2), ff.)

$$\Delta P/(\tfrac{1}{2}\rho v_r^2) = |S(\alpha)|\, S(\alpha) \tag{22}$$

where $S(\alpha)$ is given by eq. (12). This is plotted for the WCM geometry with $\beta = \beta_{max}$ in Figure 25 as a function of α for several values of Ω. Figure 21 shows the geometric relationship between angle α and distance along the blade. Quantitatively this relationship is

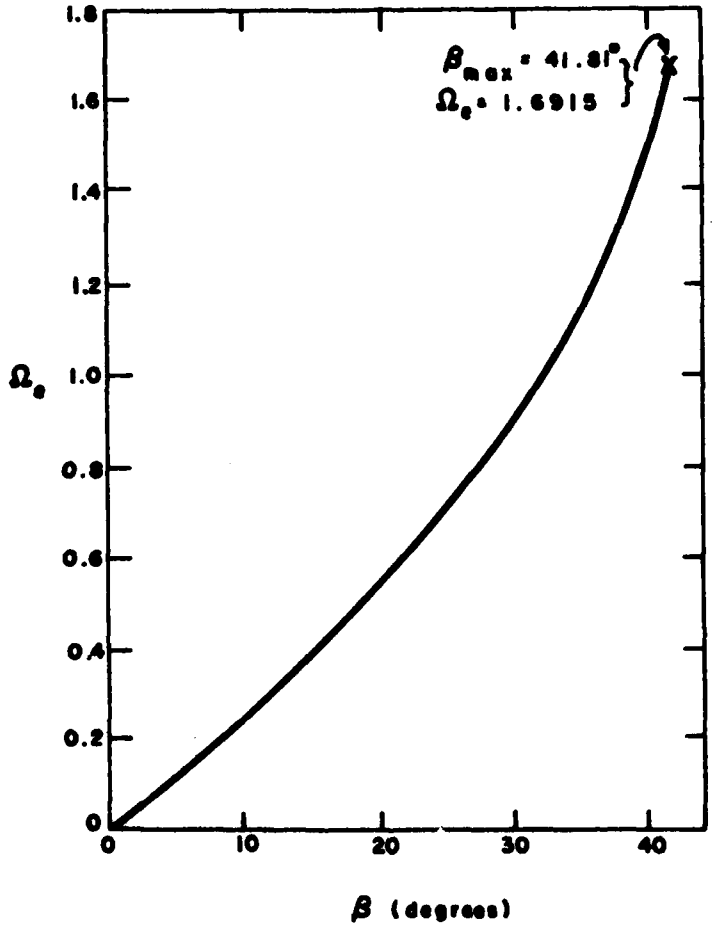

Figure 23. Nondimensional equilibrium rotation speed vs blade angle β for the WCM with constant radial flow.

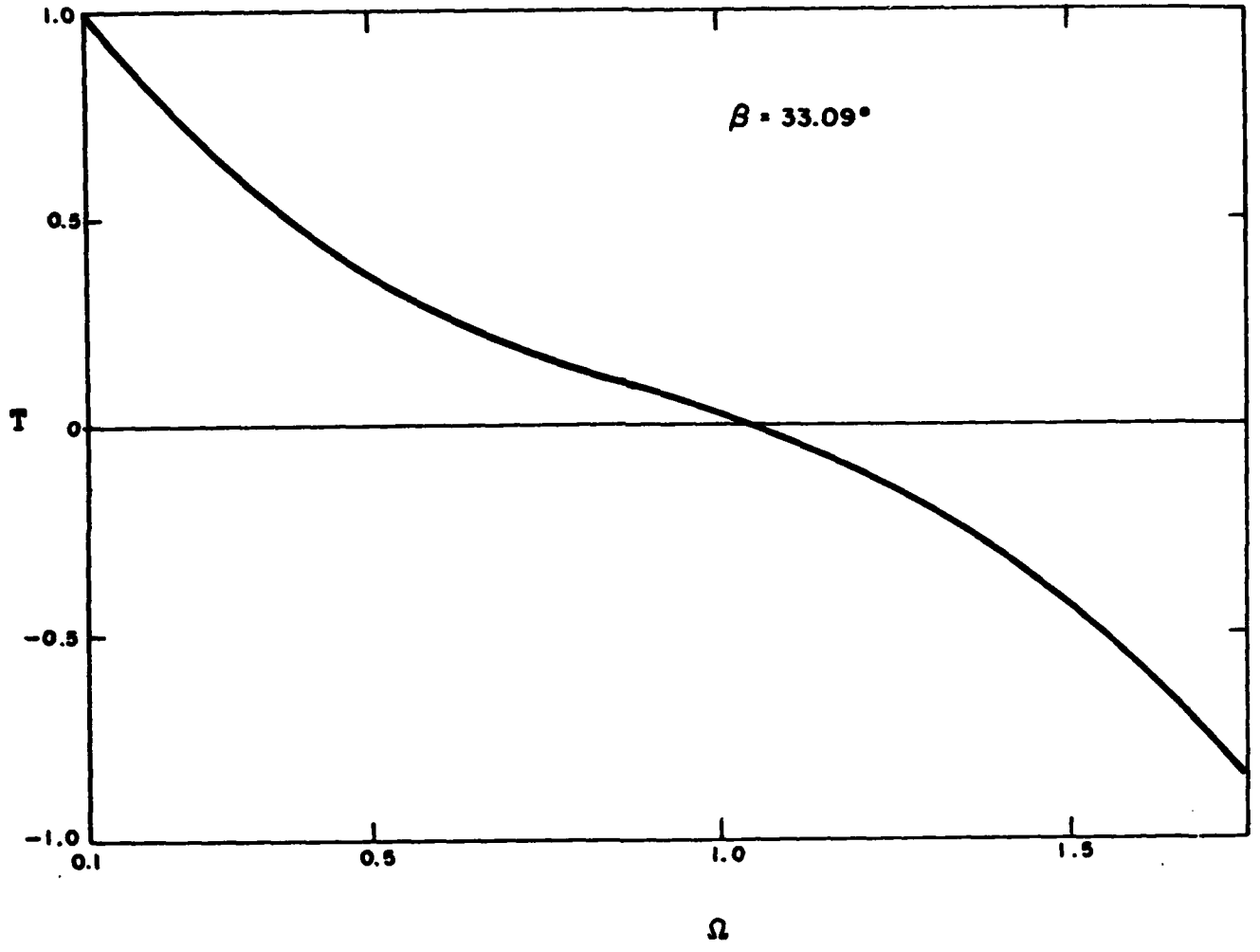

Figure 24. Nondimensional torque (eq. (13)) vs nondimensional rotation speed (eq. (11)) for the WCM with blade angle $\beta = 33.09°$. Radial flow is constant.

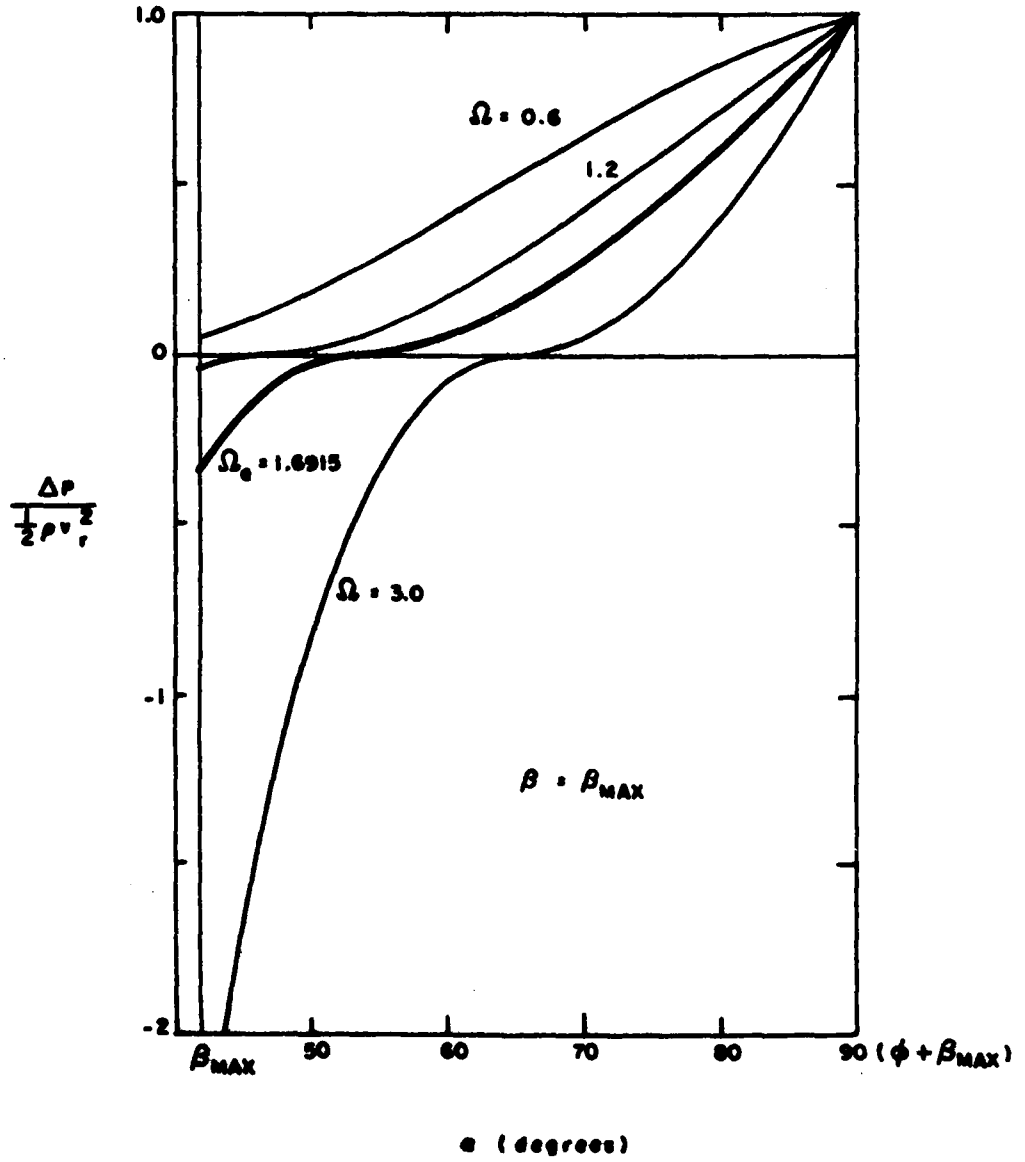

Figure 25. Dynamic pressure distributions across the length of a WCM blade oriented at maximum angle, β_{max}, for several rotation speeds. Radial flow is constant. The heavy curve is for equilibrium rotation speed. Positive pressure boosts rotation speed; negative pressure retards rotation.

$$\ell/L = \frac{\sin(\phi + \beta - \alpha)}{\sin \phi} \tag{23}$$

where ℓ is the distance along the blade from its inner end, and

$$L = r_2\cos\beta - r_1\cos(\phi + \beta). \tag{24}$$

For the WCM with $\beta = \beta_{max}$, we have $\ell = 3\cos\alpha$ cm and $L = 2.236$ cm. At the equilibrium rotation speed, the crossover from boost to drag occurs at $\alpha_o = 54.26^\circ$ ($\ell/L = 0.784$). Thus, it is apparent that torque will be increased (reduced) by, for example, decreasing (increasing) blade height toward the outer edge of the blade relative to the inner edge. Of course such a change also will affect equilibrium rotation speed in a complex manner that would have to be determined by further calculation or experiment. It should also be borne in mind that the assumption of constant v_r is unrealistic (cf. Fig. 15).

Next, we consider the more realistic assumption of linear increase of v_r with r, but use the hydrometeor spectrometer for our case study instead of the water content meter.

TOTAL TORQUE WITH LINEAR VARIATION OF RADIAL FLOW

In this case we take v_r to be zero at the inner edge of the annulus (i.e., at $r = r_1$) and v_r to be $2\bar{v}_r$ at the outer edge of the annulus (i.e., at $r = r_2$), where $\bar{v}_r$ is the mean radial speed across the annulus, and we assume linear variation of v_r between these extremes. Thus we have

$$v_r = 2\bar{v}_r\left(\frac{r - r_1}{r_2 - r_1}\right) \tag{25}$$

Using eqs. (7) and (8) this becomes

$$v_r = \frac{2\bar{v}_r}{R} \sin\beta \left[\csc\alpha - \csc(\phi + \beta)\right] \quad , \tag{26}$$

and from this result plus eqs. (4), (11) and (12) we derive

$$S(\alpha) = \frac{s}{\bar{v}_r} = \frac{2}{R} \left[\sin\beta - (1 - R)\sin\alpha\right] - \Omega \sin\beta \, \mathrm{ctn}\alpha \tag{27}$$

where

$$R = \frac{r_2 - r_1}{r_2} = \frac{\sin(\phi + \beta) - \sin\beta}{\sin(\phi + \beta)} \quad . \tag{28}$$

Corresponding to eq. (16), we have

$$\begin{aligned} D(\alpha,\Omega,\beta,R) = {} & \left(\frac{\sin\beta}{R}\right)^2 \mathrm{ctn}^2\alpha \left\{\Omega R \, \mathrm{ctn}\alpha \left[\frac{4}{3} - \frac{1}{4} \Omega R \, \mathrm{ctn}\alpha\right] - 2\right\} \\ & + 2\left(\frac{1 - R}{R}\right)\left(\frac{\sin\beta}{R}\right)\left\{4 \csc\alpha - \Omega R \left[\mathrm{ctn}\alpha \csc\alpha + \ell n(\tan\tfrac{\alpha}{2})\right]\right\} \\ & + 4\left(\frac{1 - R}{R}\right)^2 \ell n(\sin\alpha) \end{aligned} \tag{29}$$

As is the case with constant v_r, we have two situations:

1. If $\frac{S(\phi + \beta)}{S(\beta)} < 0$, the dynamic pressure reverses sign at angle α_o, where $\beta < \alpha_o < \phi + \beta$, and we compute total torque from

$$\mathbf{T} = D(\beta,\Omega,\beta,R) + D(\phi + \beta,\Omega,\beta,R) - 2D(\alpha_o,\Omega,\beta,R) \qquad (30)$$

but reverse the sign of the result if $2\sin\beta \geq \Omega\cos\beta$.

2. If $\frac{S(\phi + \beta)}{S(\beta)} > 0$, we compute total torque from

$$\mathbf{T} = D(\phi + \beta,\Omega,\beta,R) - D(\beta,\Omega,\beta,R) \qquad (31)$$

but reverse the sign of the result if $2\sin\beta \leq \Omega\cos\beta$.

In the normalization of the torque, eq. (13), we replace v_r by $\bar{v}_r$ for this case.

Calculation of α_o is not as straight forward as for the case with v_r constant. If we set eq. (27) to zero we obtain

$$\Omega\sin\beta\,\mathrm{ctn}\alpha_o + 2\left(\frac{1 - R}{R}\right)\sin\alpha_o = 2\frac{\sin\beta}{R}$$

which can be expressed as

$$\sqrt{1 + \xi^2}\,(\tfrac{1}{2}\Omega R\xi - 1) + (1 - R)/\sin\beta = 0 \qquad (32)$$

where $\xi = \mathrm{ctn}\alpha_o$. This is a quartic in ξ, with four roots, of which at least three may be real. Equation (32) is easiest solved by Newton-Raphson iteration, with care being taken to obtain the relevant root.

The hydrometeor spectrometer (HS) is used as the particular case to study these equations. Preliminary specifications for the HS are $r_1 = 5$ cm, $r_2 = 7$ cm for which we obtain (eq. (21)) $\beta_{max} = 45.585^o$. Figure 26 displays $\mathbf{T}$ vs. Ω for $\beta \approx \beta_{max}$ and $\beta = 40^o$. From the figure we find $\Omega_e(\beta_{max}) \approx 1.7825$. If we take $\bar{v}_r = 50$ m s^{-1} (see Fig. 20), then $\omega_e \approx 1273$ rad s^{-1} (1.216×10^4 RPM). Also we note that torque is comparatively insensitive to rotation speed in the neighborhood of equilibrium rotation.

Pressure distributions across the length of the blade are computed from eq. (22) with $S(\alpha)$ given by eq. (27). Results are shown in Figure 27 for $\beta = \beta_{max}$ and $\beta = 40^o$. Notice for the equilibrium rotation speeds that

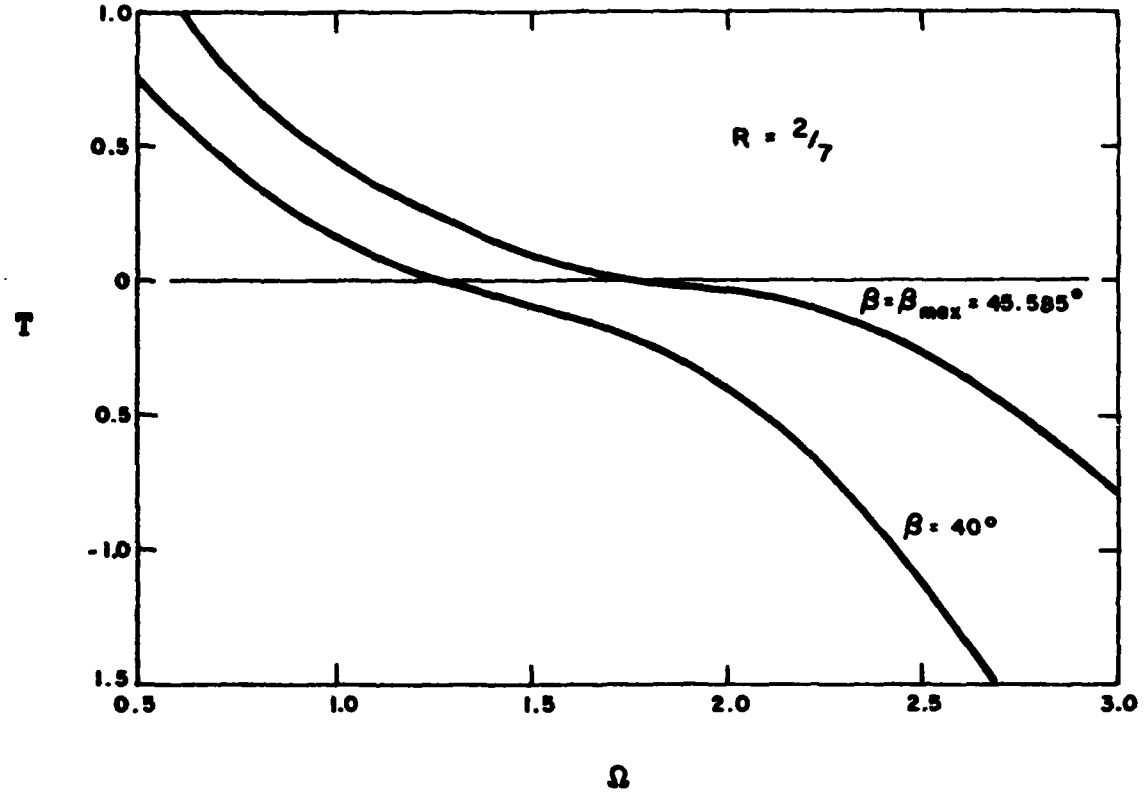

Figure 26. Nondimensional torque (eq. (13)) vs nondimensional rotation speed (eq. (11)) for the HS annulus with two values of blade angle β. Radial flow varies linearly with r.

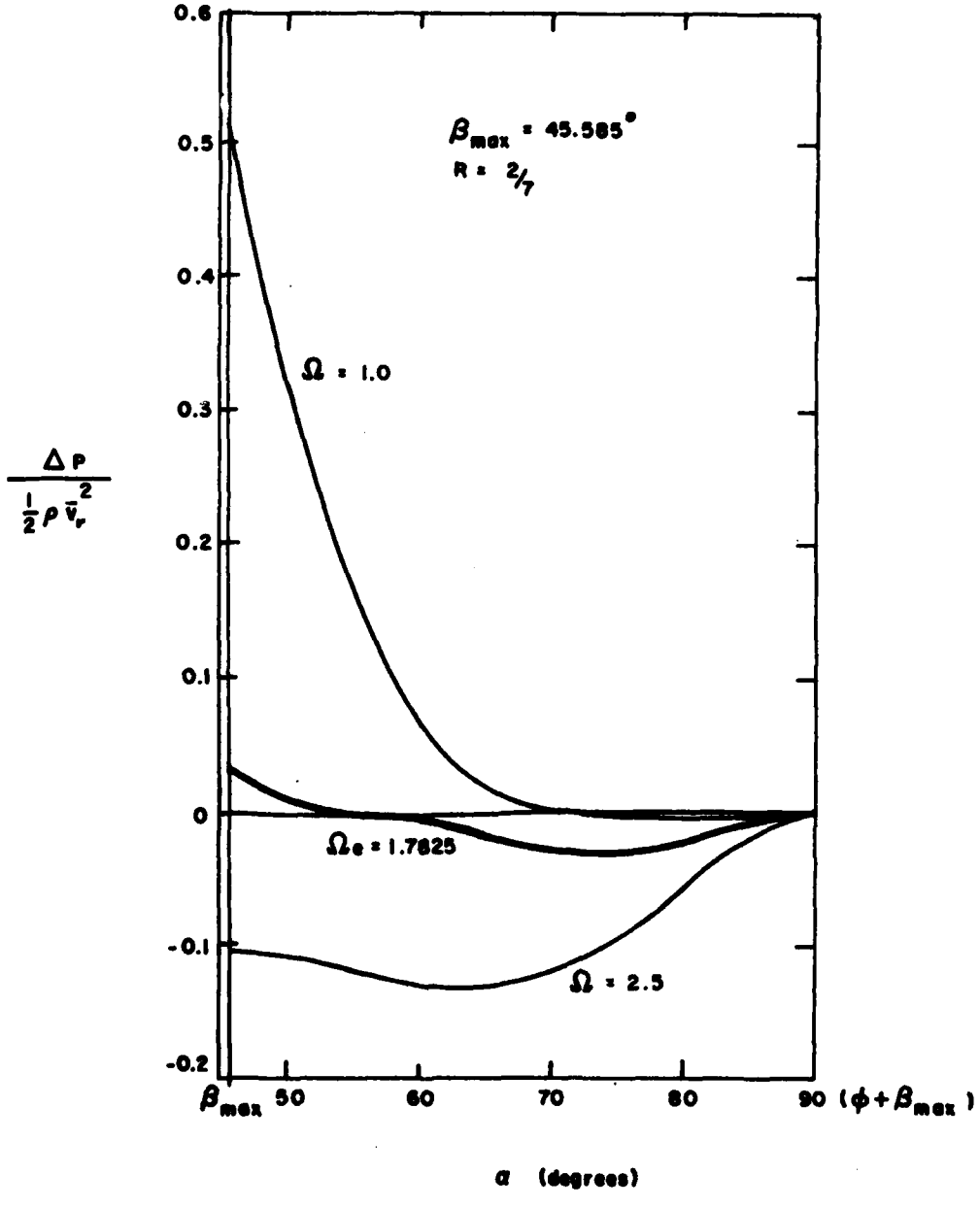

Figure 27a. Dynamic pressure distributions across the length of an HS blade oriented at maximum angle β_{max} for several rotation speeds. Radial flow varies linearly with r. The heavy curve is for equilibrium rotation speed. Positive pressure boosts rotation speed; negative pressure retards rotation.

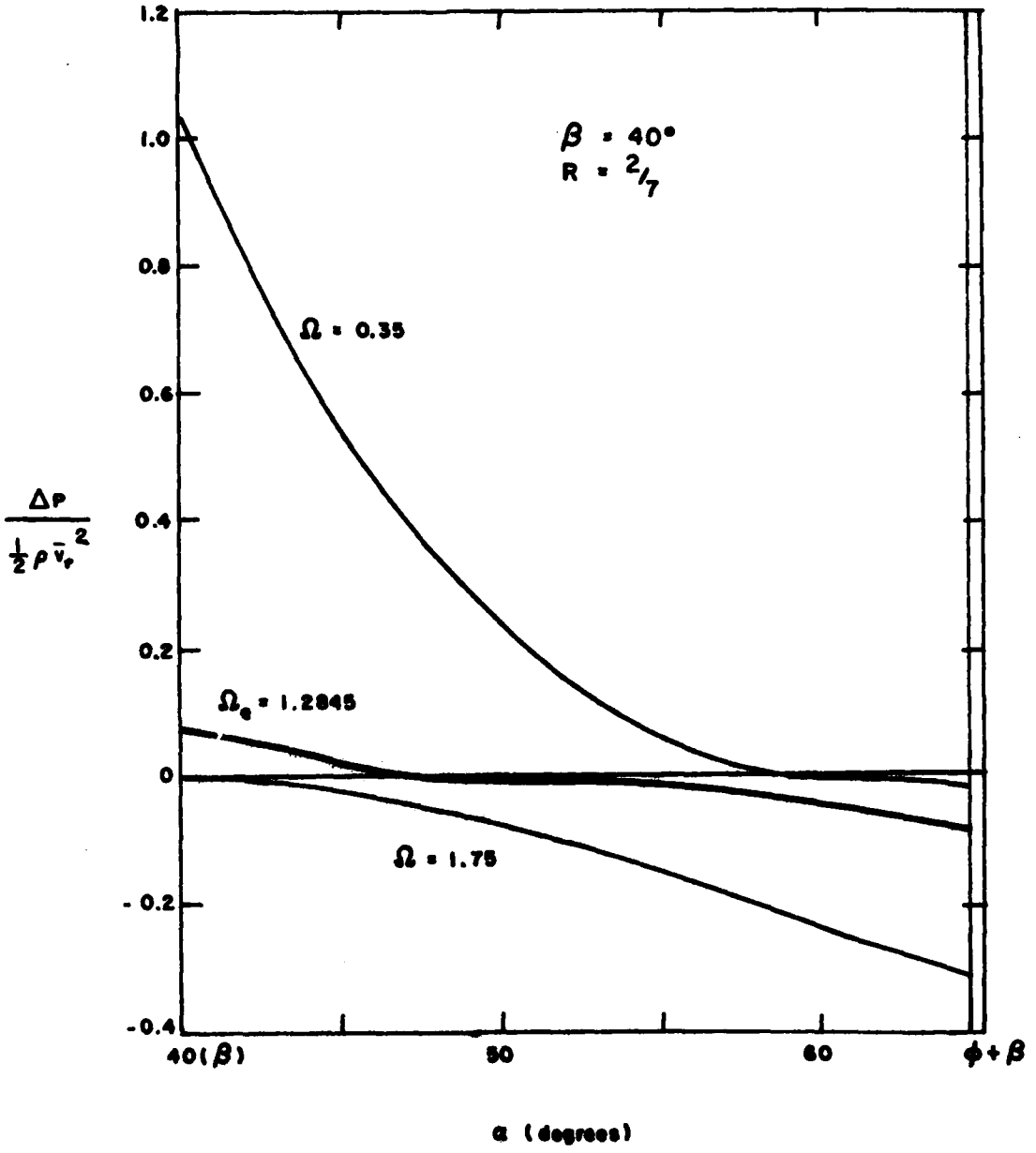

Figure 27b. Dynamic pressure distributions across the length of an HS blade oriented at maximum angle $\beta = 40^\circ$ for several rotation speeds.

Radial flow varies linearly with r. The heavy curve is for equilibrium rotation speed. Positive pressure boosts rotation speed; negative pressure retards rotation.

positive dynamic pressure, which boosts rotation, occurs toward the outer edge of the annulus, while there is drag toward the inner edge. This is precisely opposite to the situation found for the WCM meter, for which v_r is taken to be constant (cf. Fig. 25). Additional comparisons are made in the next section.

SUMMARY AND DISCUSSION

We have derived an approximate method for calculation of dynamic pressure distributions across the length of water content meter (WCM) and hydrometeor spectrometer (HS) torque blades, and total torque on the blades. Calculation of total torque requires solution of a differential equation, which has been done analytically for two simple cases:

1. Constant radial flow across the annulus face.
2. Linear variation of radial flow across the annulus face.

Blade height is taken to be constant for both cases. The first case is applied to the WCM geometry, and the second to the HS geometry.

Graphs of dimensionless total torque vs dimensionless rotation speed for the two cases are similar (cf. Figs. 24 and 26). On the other hand, comparison of the dynamic pressure distributions for equilibrium rotation for the two cases (Figs. 25 and 27), shows reverse distributions of pressure signs across the lengths of the blades for the two cases. While the geometries are somewhat different (i.e., $R_{WCM} = 0.333$ while $R_{HS} = 0.286$ (see eq. (28)), the major difference is in the radial flow as stated above, and this shows a potential for high sensitivity to change in radial flow.

We have not investigated the effect of variation of blade height on total torque or on equilibrium rotation speed. However, the pressure distribution curves indicate that at least the total torque would be

sensitive to such variation. In particular Figure 27, which is for the more realistic case, indicates that total torque would increase with increase of blade height toward the outer edge of the annulus. The effect of this change on equilibrium rotation speed is not immediately obvious.

In addition, we have not studied the effect of variation of flow in the direction normal to the annulus face. Figures 14 and 19 show that this variation in flow can be significant even without consideration of the boundary layer. Though an accurate study would require calculation of the boundary layer, useful information could be obtained by extension of the methods used in this study.

Calculations could be done with realistic variation of both blade height and flow by numerical solution of eq. (10). Sensitivities to these as well as other parameters could be studied, and the results then could be used to determine the torque blade structure that would come closest to providing the desired balance of rotation speed against torque sensitivity.

HYDROMETEOR IMPACT

INTRODUCTION

Here we are concerned with effects of hydrometeor impact other than those which are used for measurement, but which may affect instrument performance. We consider lateral jetting of impacting water drops, splash and bounce, erosion, and stress limits on torque blades imposed by collisions with water drops. We make use of the literature and some theoretical calculations; no new data are reported here.

HIGH SPEED IMPACT OF WATER DROPS: LATERAL JETTING

As a large water drop impacts at high speed on a rigid surface, a shock wave is reflected back into the drop as shown in Figure 28. Compressed water is contained between the shock front and the rigid surface until the speed of the shock front exceeds the speed of growth of the interface, after which the shock front detaches from the surface. Immediately after detachment, the pressure is relieved by a jetting of water at high speed along the rigid surface. The problem at hand is to estimate whether or not a significant amount of water might be jetted.

According to Heymann[3] the critical contact angle, ϕ_c, at which jetting begins for an impact speed* of 100 m s^{-1} is about 2.5°. However, Brunton and Camus[4] assert that Heymann's ϕ_c values are much lower than

---

3. F. J. Heymann, "High-Speed Impact Between a Liquid Drop and a Solid Surface," J. Appl. Phys. 40, 5113 (1969).

4. J. H. Brunton and J. J. Camus, "The Flow of a Liquid Drop During Impact," Proceedings of the 3rd International Conference on Rain Erosion and Associated Phenomena. A. A. Fyall and R. B. King, editors, (Elvetham Hall, 11-13 Aug. 1970). pp. 327 ff.

*Airplane cruising speed is taken here to be about 100 m s^{-1}.

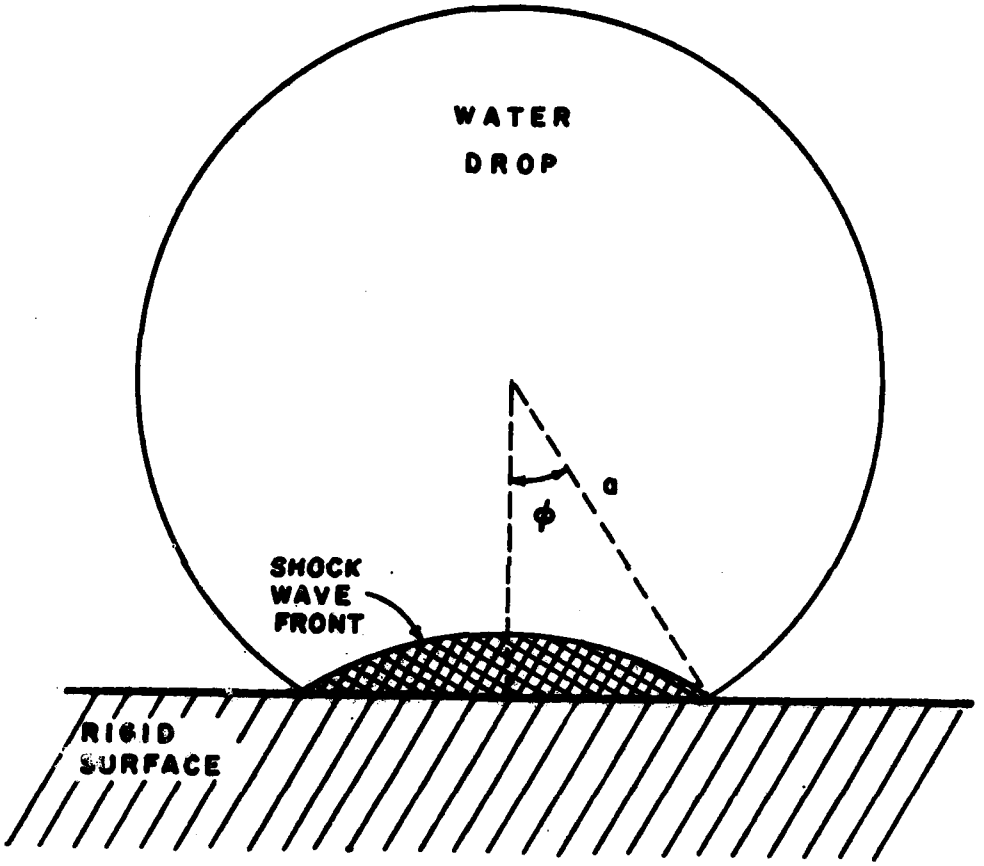

Figure 28. Development of a reflected shock front and compressed water (hatched area) during impact on a rigid surface of a large water drop.

observed, and they report values between 12° to 20°. (They also report jetting speeds of slightly higher than 1000 m s^{-1} for 100 m s^{-1} impact speed.)

Since jetting occurs only long enough to relieve the compression behind the shock front we can assume that a volume of water less than that trapped behind the shock front at $\phi = \phi_c$ will be jetted. If we assume no distortion of drop or shock front, the volume of water between the shock front and the rigid surface is simply a spherical segment of one base (see Fig. 28), and the fraction of the total drop volume involved, f, is

$$f = \tfrac{1}{4}(1 - \cos\phi_c)^2(2 + \cos\phi_c). \qquad (33)$$

For the several values of ϕ_c mentioned above we have:

ϕ_c	f
2.5°	6.8×10^{-7}
12.0°	3.6×10^{-4}
20.0°	2.7×10^{-3}

These numbers indicated that jetting is not likely to be a serious problem, though we must caution that since we have ignored the effects of rotation, the applicability of these results to the WCM and HS is questionable.

LOW SPEED IMPACT OF WATER DROPS

Normal Incidence

Mutchler and Hansen[5] present rather comprehensive experimental data on impact on stationary surfaces of large water drops at terminal

5. C. K. Mutchler and L. M. Hansen, "Splash of a Water Drop at Terminal Velocity," Science 169, 1311 (1970).

settling speeds. Their most relevant information is summarized as follows:

a. Impact on dry, smooth, hard surfaces produces no splash; the drop merely spreads horizontally.

b. Maximum splash effects occur for surface water depths of about 1/4 to 1/3 of the drop diameter.

c. Maximum splash height is about 6 times the drop diameter.

Using the data of Gunn and Kinser[6], we estimate that maximum impact speed was about 9 m s^{-1}.

Oblique Incidence

The only data found are in two papers by Taylor[7,8] on impact of identical water jets at various angles of incidence. Sketches of Taylor's results are shown in Figure 29.

After impact, the jets merge to form the thin sheets shown in the figure, where the sheets lie in the plane which bisects the angle between the jets. (This plane can be replaced by a rigid surface onto which one of the jets is impacting at an angle of θ.) Since friction and surface effects are relatively small in the region of impact of the jets, momentum conservation requires that flow speeds in the sheets be essentially equal to the jet speed. Impact pressure effects cause the sheet thickness to vary with angle ϕ. Then, when surface tension pressure at the edge of the sheet balances dynamic flow pressure (i.e., when the Weber number at the sheet edge reaches unity), the sheet breaks up into tiny droplets

---

6. R. Gunn and G. D. Kinzer, "The Terminal Velocity of Fall for Water Droplets in Stagnant Air," J. Meteor. 6, 243 (1949).

7. G. I. Taylor, "Formation of Thin Flat Sheets of Water," Proc. Roy. Soc. (London) A259, 1 (1960).

8. G. I. Taylor, "Oblique Impact of a Jet on a Plane Surface," Phil. Trans. Roy. Soc. (London) A260, 96 (1966).

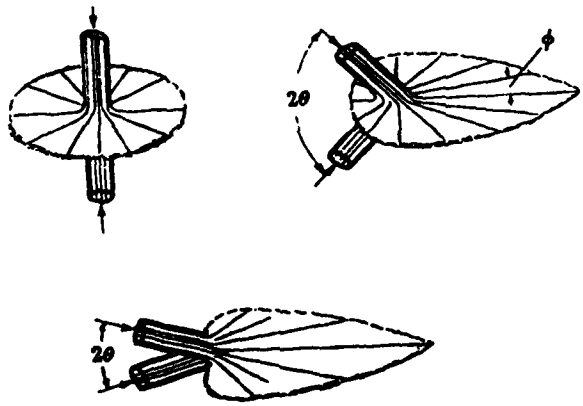

Figure 29. Sketch of sheets formed by impact of pairs of cylindrical water jets. (From ref. 7.)

which fly off tangentially to the edge of the sheet. This limits the breadth and length of the sheets as indicated in the figure.

Jet speeds of 3.6 m s^{-1} (θ = 60° and 45°) and 52 m s^{-1} (θ = 30°) were used.

MAXIMUM REBOUND DISTANCE AND RETURN TIME

To calculate maximum particle rebound after impaction and maximum return time to the surface after initial impact and rebound, we assume perfectly elastic impact. Thus, we ignore fragmentation and inelastic effects. Also, we ignore the annulus rotation and the boundary layer.

We use the results of the particle trajectory calculations to the WCM with parabolic hub (Figs. 7) to determine particle impact speeds, which are plotted in Figure 30.

Air flow components normal to the annulus surface, as computed by the Hess-Smith code for the body shown in Figure 6 at a distance of r = 2.4 cm from the WCM axis, were used in the particle trajectory calculations. This flow, v_x/V_∞, was found to be closely fit by the equation

$$\eta = \zeta\left[1 \pm \sqrt{1 + (0.215/\zeta)^2}\right] \tag{34}$$

where

$$\eta = \log_{10}(v_x/V_\infty)$$

$$\zeta = \tfrac{1}{2}\left[\log_{10}(-x/r_2) + 0.518\right]$$

and the + sign is taken if ζ is minus while the - sign is taken if ζ is positive.

Initial particle rebound speeds were taken from Figure 30, and were directed in the minus x direction. Air flow was calculated from eq. (34).

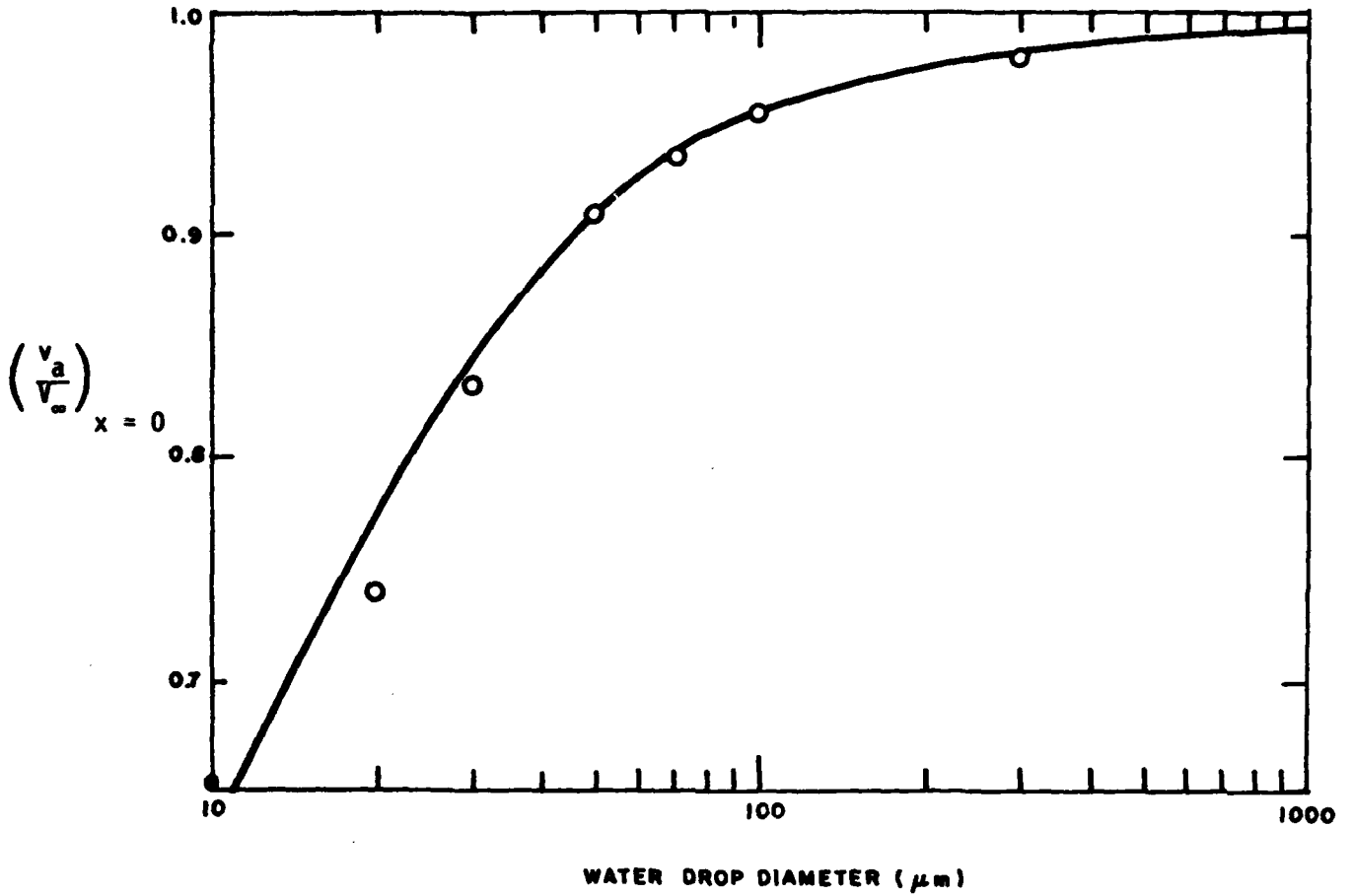

Figure 30. Calculated water drop impact speeds, v_a, on the disc annulus with parabolic hub (see Figs. 7) at r = 2.4 cm. V_∞ = 100 m s^{-1}.

Trajectories were calculated for spheres by use of the methods described in reference 1, except that gravity was ignored. Atmospheric conditions for 3 km altitude in the U. S. Standard Atmosphere were used:

$T = 268.66^{\circ}$ K

$P = 70121$ Pa

$\rho = 0.90925$ kg m^{-3}

$\eta = 1.6938 \times 10^{-5}$ kg m^{-1} s^{-1}

Free stream air speed, V_{∞}, was taken to be 100 m s^{-1}. Particle densities of 917 kg m^{-3} (ice), and 100 kg m^{-3} (snow) were used. Results are listed in Table 1.

EROSION

Water Drops

According to Brunton and Camus[4], surface erosion in the form of "small, shallow depressions or dimples" begins to appear on stainless steel after about 1000 water drop impacts at 125 m s^{-1}. From this, and other data presented in the Proceedings of the Third International Conference on Rain Erosion and Associated Phenomena[4], it appears that at the comparatively low impact speeds of interest here there would not be an immediate erosion problem. However, after extended use, the instrument surfaces probably would become roughened by erosion, particularly if constructed of a soft metal such as aluminum.

Parker makes an observation of interest in his addendum to reference 4. He found that surface roughness causes a marked decrease in water drop retention on a rotating surface. Moreover, he shows sketches of disintegration of an impacted water drop into small droplets after low-speed impact on a rotating surface, the disintegration presumably being caused by surface roughness.

TABLE 1

MAXIMUM PARTICLE REBOUND DISTANCES AND RETURN TIMES

a. Particle density 917 kg m^{-3}

Particle Diameter (μm)	Initial Rebound Velocity ($m\ s^{-1}$)	Max. Rebound Distance (cm)	Time at Max. Rebound Distance (s)	Return Time (s)	Final Velocity ($m\ s^{-1}$)
10	- 63.0	- .403	1.485×10^{-4}	4.38×10^{-4}	13.2
20	- 74.0	- .921	2.700	7.26	24.1
40	- 88.4	- 2.116	5.400	1.38×10^{-3}	33.7
70	- 93.7	- 4.252	1.05×10^{-3}	2.64	38.9
100	- 95.6	- 6.469	1.62	4.04	40.4
200	- 97.5	- 13.93	3.54	8.88	41.1
400	- 98.5	- 28.86	7.44	1.87×10^{-2}	41.2
700	- 98.9	- 51.08	1.32×10^{-2}	3.34	41.3
1000	- 99.2	- 73.28	1.89	4.80	41.4
2000	- 99.5	-146.7	3.78	9.63	41.6
4000	-100.0	-293.7	7.56	1.927×10^{-1}	41.8
7000	-100.0	-511.8	1.32×10^{-1}	3.36	41.9

b. Particle density 100 kg m^{-3}

Particle Diameter (μm)	Initial Rebound Velocity ($m\ s^{-1}$)	Max. Rebound Distance (cm)	Time at Max. Rebound Distance (s)	Return Time (s)	Final Velocity ($m\ s^{-1}$)
10	- 63.0	- .076	4.05×10^{-5}	3.48×10^{-4}	0.11
20	- 74.0	- .206	8.10×10^{-4}	3.09	5.56
40	- 88.4	- .462	1.32×10^{-4}	4.30	15.2
70	- 93.7	- .811	2.01	5.94	23.2
100	- 95.6	- 1.15	2.76	7.70	28.0
200	- 97.5	- 2.14	5.16	1.37×10^{-3}	33.5
400	- 98.5	- 3.97	9.60	2.54	36.4
700	- 98.9	- 6.58	1.63×10^{-3}	4.24	37.9
1000	- 99.2	- 9.15	2.28	5.93	38.6
2000	- 99.5	- 17.52	4.44	1.14×10^{-2}	39.7
4000	-100.0	- 34.08	8.76	2.23	40.5
7000	-100.0	- 58.5	1.51×10^{-2}	3.83	40.9

Ice Particles

The question here is whether significant erosion is to be expected from impact of large single-crystals of ice at impact speeds of about 100 m s^{-1}. We have not succeeded in finding specific data with which to answer this question. There are, however, good general discussions and some interesting data in the book by Engle[9]. Here we summarize some of Engle's more pertinent discussions.

Impact surface damage is caused by the immediate effects of the collision (primary erosion), and also by secondary collisions of fragments (secondary erosion). Thus, the dent or pit caused by the primary erosion is usually surrounded by the many smaller scars of the secondary erosion. Primary erosion damage on ductile surfaces is usually a maximum at angles of incidence between 20-30°, but secondary erosion reaches a maximum at 90° incidence.

For normal incidence, erosion is independent of particle size over a considerable range of sizes.

It has been found that weaker, fragile particles sometimes produce greater erosion than stronger particles. This is caused by fragmentation where the secondary particles remove lips formed by primary impact.

Summary

At the impact speed of about 100 m s^{-1} under consideration here, it is apparent that water drops will not cause significant surface erosion except perhaps after extended exposure. In the case of large ice particles, however, we cannot be assured that erosion will be insignificant, expecially if a comparatively soft metal such as aluminum is used. Moreover, we can

---

9. P. A. Engel, Impact Wear of Materials (Elsevier, 1976). Chapter 5.

expect that surface roughness caused by erosion will alter the retention characteristics of the instrument surfaces, and thereby affect instrument performance.

IMPACT STRESS ON THE TORQUE BLADES

We are concerned here with the force of impact, and resulting impact stress, of large water drops on the sides of the torque blades. Impact is caused by rotation of the blades into the water drops. The questions to be answered are: how much impact stress is generated in the blades; which candidate construction metals are satisfactory and which are not; and how thick must the blades be to reduce the stress to tolerable levels?

Force of Impact of a Large Water Drop

A plan view of the overall annulus and blade geometry is shown in Figure 21, and details of the WCM blade geometry are shown in Figure 11. From Figure 21 and eq. (11), it is apparent that the maximum impact speed, v_i, is

$$v_i = \omega r_2 \cos\beta = v_r \Omega \cos\beta \quad . \tag{35}$$

According to Heymann[3] the peak impact pressure of a large drop is approximately

$$P_{max} \approx 2.8 \rho_w C_w v_i$$

where ρ_w is water density and C_w is speed of sound in water. However, this seems to be localized at the periphery of the impact area, while at the center of the impact area, the pressure is closer to

$$P_{center} \simeq \rho_w C_w v_i \quad .$$

For this calculation we will use a simple average of these equations for the impact pressure, P_i,

$$P_i \simeq 1.4 \rho_w C_w v_i \quad . \tag{36}$$

Critical contact angle, ϕ_c, may be defined as the contact angle (Fig. 28) at peak pressure. From Figure 28 the contact area at peak pressure, A_i, is

$$A_i = \pi \, (a \sin \phi_c)^2 \quad , \tag{37}$$

where a is drop radius. Thus the impact force, $F_i = P_i A_i$, is given, on combining eqs. (35)-(37), by

$$F_i \simeq 1.4\pi \, P_w C_w a^2 v_r \Omega \sin^2 \phi_c \cos\beta \quad . \tag{38}$$

Maximum Stress on the Blade

Standard engineering methods used for calculation of maximum stress in a beam can be used here[10]. Geometry and notation are shown in Figure 31. The impact force causes the blade to bend, which sets up stress forces, S, in the blade which act parallel to the surface of the blade as shown in the Figure. On the convex (upper) surface of the bent blade, the stress is caused by stretching, while on the concave (lower) surface, the stress is caused by compression. At the surfaces, the stresses are at their maxima and are designated as S_m. For our blade of height h, width L and thickness δ, the maximum stress is

10. E. Hausmann and E. P. Slack, Physics (D. Van Nostrand, 3rd Edition, 1948). Secs. 107-108.

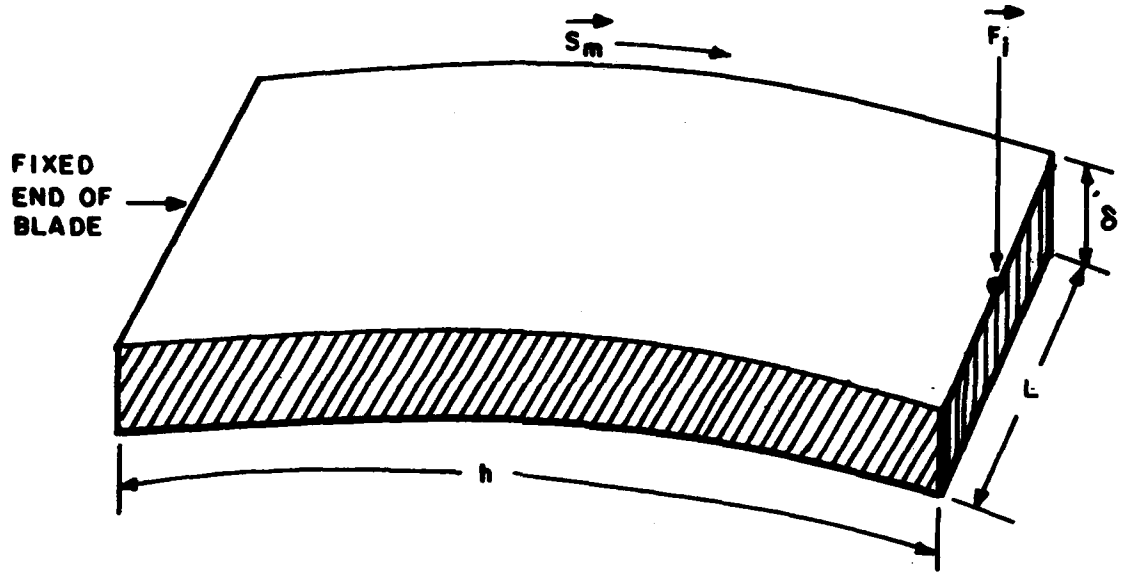

Figure 31. Geometry of a bent beam or blade showing the relationship of the impact and stress force vectors.

$$S_m = \frac{M\delta}{2I} \tag{39}$$

where

$$M = F_i h \tag{40}$$

is the bending moment, and I is the moment of inertia of the blade crossection area, given by

$$I = L\delta^3/12 \tag{41}$$

for a blade of rectangular crossection.

Combining eqs. (38)-(41) we have, finally,

$$S_m = 8.4\pi\ \rho_w C_w a^2 v_r \Omega \cos\beta \sin^2\phi_c \left(\frac{h}{L\delta^2}\right) \tag{41}$$

For the WCM we can use $\beta = \beta_{max}$ and $\Omega_e = 1.6915$ (Fig. 23). From Figure 14, we take $v_r = 80 \text{m s}^{-1}$ as a reasonably conservative typical value. Brunton and Camus[4] report that ϕ_c is in the range 12-20°; we use $\phi_c = 15°$ here. Other quantities are $\rho_w = 1000 \text{ kg m}^{-3}$ and $C_w = 1500 \text{ m s}^{-1}$.

From Figure 11, we see that the height of the tall portion of the WCM blade is 5 mm. To allow for full impact of large water drops near the end of the blade, we take h = 4 mm. The width of the tall portion of the blade is roughly L = 6 mm. Thus, in terms of water drop radius and blade thickness, we obtain

$$S_m = \begin{cases} 1.783 \times 10^8 (a/\delta)^2 & (\text{N m}^{-2}) \\ 1.783 \times 10^9 (a/\delta)^2 & (\text{dynes cm}^{-2}) \\ 2.586 \times 10^4 (a/\delta)^2 & (\text{psi}) \end{cases} \tag{42}$$

Equation (42) is plotted in Figure 32.

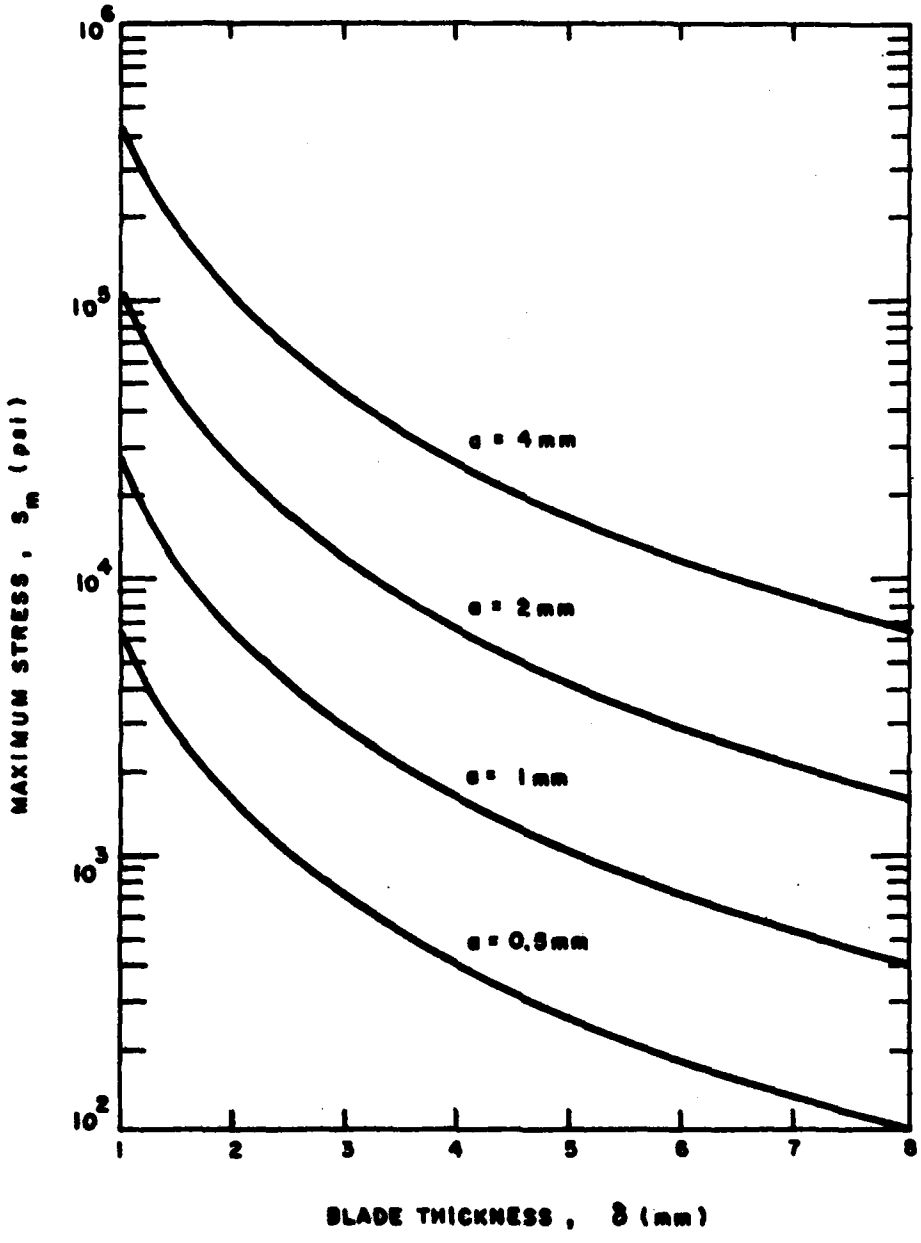

Figure 32. Maximum tensil stress vs. blade thickness for impact of water drops of radius a according to eq. (42).

Yield Strength and Tensil Strength of Metals

Tensil and yield strengths of metals are determined by applying stretching forces to bars of metal and measuring the linear stretch as a function of applied force. The tensil stress, S, is defined as

S = Force/original crossectional area of bar.

This is plotted against strain, s, which is defined as

s = Increase in length of bar/original length of bar.

A typical stress-strain curve is shown in Figure 33. The elastic range, over which the bar returns to its original length when the load is released, is the range of applicability of Hook's law. Yield strength is defined to be the tensil stress at a point at which the permanent set (i.e., permanent stretch) is 0.2% of the original bar length. Tensil strength is the maximum tensil stress on the curve. (Tensil strength is also called "ultimate tensil stress" or "ultimate strength.")

For our purposes, yield strength can be considered to be the stress at which permanent deformation begins to occur, and tensil strength the stress at which total failure occurs.

To ensure a margin of safety, safety-factor multiples (i.e., design factors) are customarily applied to instrument and machine designs. That is, the design is such that the maximum stress in the device will be a fraction 1/N of the yield strength or tensil strength of the construction material, where N is the safety factor. According to Faires[11], the following are traditional values of N for steel and ductile metals:

---

11. V. M. Faires, Design of Machine Elements (MacMillan, 1965). Table 1.1

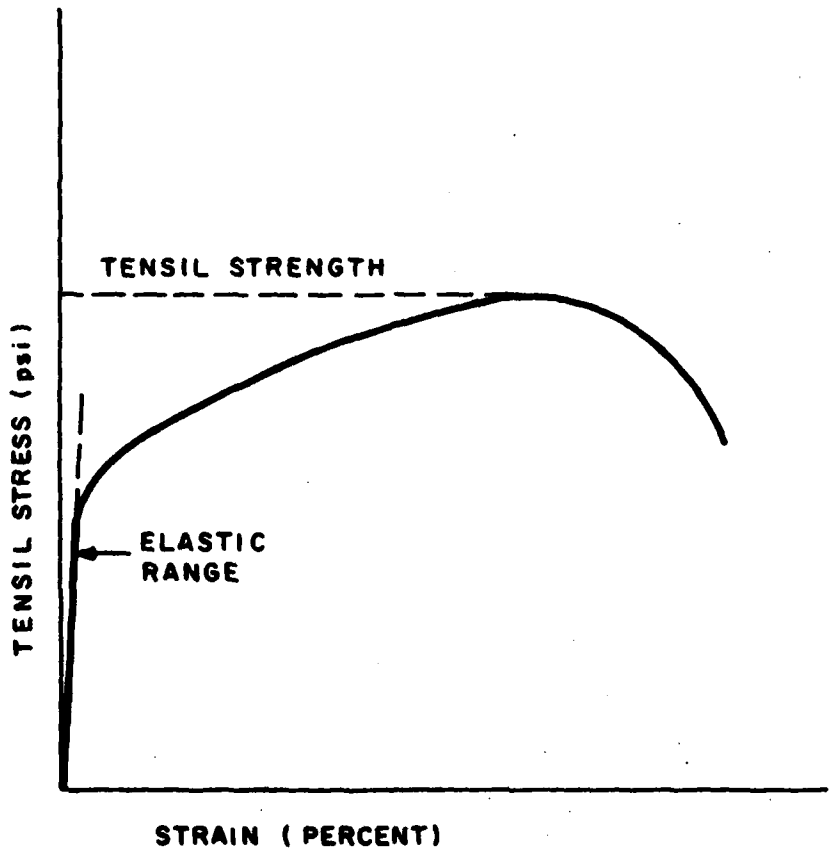

Figure 33. Typical stress-strain curve.

Kind of Load	N — Based on Yield Strength	N — Based on Tensil Strength
Dead load	3-4	1.5-2
Repeated, unidirectional, gradual, mild shock	6	3
Repeated, reversed, gradual, mild shock	8	4
Shock	10-15	5-7

The last row, for shock, would be the one applicable here. Thus, the blades should be constructed of a metal that has a tensil strength 5-7 times the stress values computed by eqs. (41) or (42), or shown in Figure 32.

Table 2 gives yield strength, tensil strength and some other data for aluminum, titanium, several strong alloys of aluminum and titanium, and for a strong stainless steel. Consider aluminum with a tensil strength of 13,000 psi. This should be 5-7 times the maximum stress in the blades, and from Figure 32, we find that blades of unreasonable thickness would be required. Aluminum alloys are considerably stronger, but still inadequate. Titanium alloys and stainless steel, with tensil strengths on the order of 150,000 psi, would require blade thickness of about 3 mm, including a conventional safety margin, to withstand collision with the larger drops.

Summary and Conclusions

Maximum stresses, caused by impact with large water drops, in the tall portion of the WCM blade design shown in Figure 11 are plotted in Figure 32. Maximum stress varies with the square of the ratio of water drop radius to blade thickness.

TABLE 2

PROPERTIES OF METALS AND ALLOYS

Metal or Alloy	Tensil Strength (psi)	Yield Strength (psi)	Youngs Modulus (psi)	Hardness: RC-Rockwell C BHN-Brinell	Ref
Pure Aluminum - Annealed	13,000	5,000	$1X10^7$		12
Aluminum Alloy, 7075T6 - Heat Treated	76,000	67,000	$1.04X10^7$		12
Wrought	82,000	72,000			13
Aluminum Alloy, 1100-H18 - Wrought	24,000	21,000			13
Aluminum Alloy, 122-T61 - Sand Casting	36,000	30,000			13
Pure Titanium - Annealed	59,000	40,000	$1.5X10^7$		12
			$1.65X10^7$		14
Ti-Al(6)-V(14)α-β - Heat Treated	170,000	150,000	$1.5X10^7$		12
Ti-Cr-Fe-Mo, Ti-140A - Heat Treated	155,000	145,000	$1.65X10^7$	342 BHN	14
	150,000	140,000			13
Ti-Al-Fe-Cr-Mo, Ti-155A - Heat Treated	160,000	150,000	$1.65X10^7$	362 BHN	14
	150,000	140,000		38 RC	13
Stainless Steel, - Quenched and Drawn to 1300°F	90,000	35,000	$3X10^7$	135 BHN	14
.12 C, 18.0 Cr, 8.0 Ni Quenched and Drawn to 800°F	200,000	150,000		380 BHN	14

Aluminum and aluminum alloys are found to lack sufficient tensil strength to be used for the blades (Table 2). Titanium alloys and strong stainless steel, which have tensil strengths on the order of 150,000 psi, are adequate. Including a safety margin factor of about 5, a blade thickness of about 3 mm should be adequate.

APPENDIX A

GLOSSARY OF SYMBOLS

a	water drop radius
C_w	speed of sound in water
$D(\alpha,\Omega,\beta,R)$	defined by eq. (29)
E	particle impaction efficiency
$\vec{F}$	dynamic pressure force on a torque blade
h	blade height
HS	hydrometeor spectrometer
L	torque blade length
P_i	water drop impact pressure
ΔP	dynamic pressure
r	radial coordinate in an axially symmetric system with the symmetry axis in the x coordinate direction
r_1	inner radius of the annular collection surface
r_2	outer radius of the annular collection surface
R	radius of a simple disc particle collector, or see eq. (28)
s	defined by eq. (4), or strain
$S(\alpha)$	defined by eqs. (12) and (27)
T	torque
$\mathbf{T}$	nondimensional torque (eq. (13))
$\vec{v}$	flow vector

v_i	maximum impact speed of a water drop on the side of a torque blade
v_p	component of flow normal to the blade surface
v_r	radial component of flow velocity
v_x	x component of flow velocity
V_∞	free stream air speed
WCM	cloud water content meter
x	streamwise coordinate, positive in the downstream direction with origin at the collection surface
α	angle between the torque blade and the radial direction
α_o	angle between the torque blade and radial axis which defines the point along the blade at which the dynamic pressure is zero
β	angle of the torque blade with the radial axis at $r = r_2$
δ	torque blade thickness (see Fig. 31)
ρ	air density
ρ_w	water density
$\gamma(\alpha,\Omega,\beta)$	defined by eq. (16)
ϕ_c	critical contact angle of water drop during impact on a rigid surface (see Fig. 28)
ω	angular rotation speed of the annulus
ω_e	equilibrium angular rotation speed of the annulus
Ω	nondimensional angular rotation speed (eq. (11))
Ω_e	equilibrium nondimensional angular rotation speed

APPENDIX B

NEWTON-RAPHSON CALCULATION OF EQUILIBRIUM ROTATION SPEED

We express rotation rate in terms of the dimensionless rotation speed Ω (eq. (11)), and we take both h and v_r to be constant. Our objective is to find Ω such that $\mathbf{T}$ (eq. (18)) is zero. We begin with an initial estimate of Ω, Ω_1, and after i - 1 Newton-Raphson iterations we calculate the $i + 1^{th}$ estimate of Ω from the equation

$$\Omega_{i+1} = \Omega_i - \mathbf{T}_i/(d\mathbf{T}/d\Omega)_i \tag{1A}$$

Iteration continues until $\mathbf{T}$ differs from zero by no more than an acceptable tolerance.

Given Ω_i, we can calculate $\mathbf{T}_i$ from eq. (18), and it remains to derive an expression for $d\mathbf{T}/d\Omega$. This can be shown to be

$$\frac{1}{\sin^2\beta}\frac{d\mathbf{T}}{d\Omega} = -2\mathrm{ctn}\alpha_o\left(1 - \Omega\sin\beta\,\mathrm{ctn}\alpha_o\csc\alpha_o\right)^2\frac{d\alpha_o}{d\Omega}$$

$$+\tfrac{1}{2}\Omega\sin^2\beta\left[2\mathrm{ctn}^4\alpha_o - \mathrm{ctn}^4\beta - \mathrm{ctn}^4(\phi+\beta)\right]$$

$$-\sin\beta\left[\frac{2\mathrm{ctn}\alpha_o}{\sin\alpha_o} - \frac{\mathrm{ctn}\beta}{\sin\beta} - \frac{\mathrm{ctn}(\phi+\beta)}{\sin(\phi+\beta)} + \ell n\left\{\frac{\tan^2(\alpha_o/2)}{\tan(\beta/2)\tan(\frac{\phi+\beta}{2})}\right\}\right] \tag{2A}$$

where

$$\frac{d\alpha_o}{d\Omega} = \frac{\tan\alpha_o\sin^2\alpha_o}{\Omega^3\sin^2\beta\sqrt{1 + (2/\Omega\sin\beta)^2}} \tag{3A}$$

REFERENCES

1. H. G. Norment, "Calculation of Water Drop Trajectories to and About Arbitrary Three-Dimensional Bodies in Potential Airflow," Atmospheric Science Associates, NASA CR 3291 (August 1980). N80-28302

2. J. L. Hess and A. M. O. Smith, "Calculation of Non-Lifting Potential Flow About Arbitrary Three-Dimensional Bodies," McDonnell Douglas Report E. S. 40622 (15 March 1962). AD-282 255

3. F. J. Heymann, "High-Speed Impact Between a Liquid Drop and a Solid Surface," J. Applied Phys. 40, 5113 (1969).

4. J. H. Brunton and J. J. Camus, "The Flow of a Liquid Drop During Impact," Proceedings of the 3rd International Conference on Rain Erosion and Associated Phenomena, A. A. Fyall and R. B. King, editors, (Elvetham Hall, 11-13 Aug. 1970). pp. 327ff.

5. C. K. Mutchler and L. M. Hansen, "Splash of a Waterdrop at Terminal Velocity," Science 169, 1311 (1970).

6. R. Gunn and G. D. Kinzer, "The Terminal Velocity of Fall for Water Droplets in Stagnant Air," J. Meteor. 6, 243 (1949).

7. G. I. Taylor, "Formation of Thin Flat Sheets of Water," Proc. Roy. Soc. (London) A259, 1 (1960).

8. G. I. Taylor, "Oblique Impact of a Jet on a Plane Surface," Phil. Trans. Roy. Soc. (London) A260, 96 (1966).

9. P. A. Engel, Impact Wear of Materials (Elsevier, 1976). Chapter 5.

10. E. Hausmann and E. P. Slack, Physics (D. Van Nostrand, 3rd Edition, 1948). Secs. 107-108.

11. V. M. Faires, Design of Machine Elements (MacMillan, 1965). Table 1.1

12. H. A. Rothbart, editor, Mechanical Design and Systems Handbook (McGraw-Hill, 1964). p. 17-4.

13. T. Baumeister and L. S. Marks, editors, Standard Handbook for Mechanical Engineers, 7th Edition (McGraw-Hill, 1967). pp. 6-90, 6-100, 6-101.

14. V. L. Doughtie, A. Vallance and L. F. Kreisle, Design of Machine Members (McGraw-Hill, 1964). pp. 31, 43


DATE
ILME